



## Research paper

# Identification of 1,2,3-triazolium salt-based inhibitors of *Leishmania infantum* trypanothione disulfide reductase with enhanced antileishmanial potency *in cellulo* and increased selectivity

Héctor de Lucio<sup>a,1</sup>, Alejandro Revuelto<sup>b,1</sup>, Alejandra A. Carriles<sup>c</sup>, Sonia de Castro<sup>b</sup>, Sonia García-González<sup>b</sup>, Juan Carlos García-Soriano<sup>a</sup>, Mercedes Alcón-Calderón<sup>a</sup>, Pedro A. Sánchez-Murcia<sup>d</sup>, Juan A. Hermoso<sup>c</sup>, Federico Gago<sup>e,f</sup>, María-José Camarasa<sup>b</sup>, Antonio Jiménez-Ruiz<sup>a,f,\*\*</sup>, Sonsoles Velázquez<sup>b,\*</sup>

<sup>a</sup> Universidad de Alcalá, Departamento de Biología de Sistemas, 28805 Alcalá de Henares, Madrid, Spain

<sup>b</sup> Instituto de Química Médica (IQM), CSIC, Juan de la Cierva 3, 28006, Madrid, Spain

<sup>c</sup> Department of Crystallography and Structural Biology, Institute of Physical Chemistry "Rocasolano" (IQFR-CSIC), 28006, Madrid, Spain

<sup>d</sup> Division of Physiological Chemistry, Otto Loewi Research Center, Medical University of Graz, Neue Stiftingtalstraße 6/III, 8010, Graz, Austria

<sup>e</sup> Universidad de Alcalá, Área de Farmacología, Departamento de Ciencias Biomédicas, 28805 Alcalá de Henares, Madrid, Spain

<sup>f</sup> Laboratorio de Modelado Molecular, Unidad asociada al CSIC por el IQM, 28805 Alcalá de Henares, Madrid, Spain



## ARTICLE INFO

## Keywords:

N-alkylation  
1,2,3-Triazolium salts  
Trypanothione disulfide reductase  
*Leishmania infantum*  
Competitive inhibitor  
Dimerization disruptor

## ABSTRACT

N-methylation of the triazole moiety present in our recently described triazole-phenyl-thiazole dimerization disruptors of *Leishmania infantum* trypanothione disulfide reductase (LiTryR) led to a new class of potent inhibitors that target different binding sites on this enzyme. Subtle structural changes among representative library members modified their mechanism of action, switching from models of classical competitive inhibition to time-dependent mixed noncompetitive inhibition. X-ray crystallography and molecular modeling results provided a rationale for this distinct behavior. The remarkable potency and selectivity improvements, particularly against intracellular amastigotes, of the LiTryR dimerization disruptors **4c** and **4d** reveal that they could be exploited as leishmanicidal agents. Of note, *L. infantum* promastigotes treated with **4c** significantly reduced their low-molecular-weight thiol content, thus providing additional evidence that LiTryR is the main target of this novel compound.

## 1. Introduction

Leishmaniasis encompasses a group of infectious diseases caused by protozoan parasites from the genus *Leishmania* that are transmitted to the human host through the bite of infected female *Phlebotomus* spp. or *Lutzomyia* spp. sandflies. The main clinical presentations are cutaneous, mucocutaneous and visceral. Visceral leishmaniasis (VL) –also known as kala-azar– is the most severe form of the disease, which leads to death in over 95% of untreated cases. According to the World Health Organization [1], the estimated incidence of VL oscillates between 50,000 and 90,000 new cases per year worldwide. High VL burden regions include the Indian subcontinent, East Africa, South America and China,

where the causative agents of VL, *Leishmania donovani* and *Leishmania infantum*, are endemic and mainly affect socially and economically disadvantaged human populations [1,2].

Although several vaccine candidates are presently undergoing different stages of clinical evaluation, chemotherapy is still the main option to control all forms of this disease [3]. However, the drugs currently approved against leishmaniasis have significant drawbacks, such as high toxicity and long-term and complicated treatment regimens, which lead to the appearance of undesirable side effects and drug-resistant parasites [3–5]. Therefore, there is a pressing demand to discover new effective drugs against leishmaniasis, especially in its most lethal visceral form.

The life cycle of *Leishmania* parasites comprises two developmental

\* Corresponding author. Instituto de Química Médica (IQM-CSIC), c/ Juan de la Cierva 3 E-28006, Madrid, Spain.

\*\* Corresponding author. Departamento de Biología de Sistemas, Universidad de Alcalá, E-28805 Alcalá de Henares, Madrid, Spain.

E-mail addresses: [antonio.jimenez@uah.es](mailto:antonio.jimenez@uah.es) (A. Jiménez-Ruiz), [iqmsv29@iqm.csic.es](mailto:iqmsv29@iqm.csic.es) (S. Velázquez).

<sup>1</sup> These two authors contributed equally to this work.

<https://doi.org/10.1016/j.ejmech.2022.114878>

Received 15 July 2022; Received in revised form 14 October 2022; Accepted 21 October 2022

Available online 29 October 2022

0223-5234/© 2022 The Authors. Published by Elsevier Masson SAS. This is an open access article under the CC BY-NC-ND license (<http://creativecommons.org/licenses/by-nc-nd/4.0/>).

### Abbreviations

BSO	D,L-buthionine-(S,R)-sulfoximine
CC <sub>50</sub>	half-maximal cytotoxic concentration
CCTLC	centrifugal circular thin layer chromatography
DTNB	5,5'-dithiobis-(2-nitrobenzoic acid)
EC <sub>50</sub>	half maximal effective concentration
HepG2	liver hepatocellular carcinoma
HPFC	high performance flash column chromatography
IC <sub>50</sub> <sup>act</sup>	half-maximum inhibitory concentration in the oxidoreductase activity assay
IC <sub>50</sub> <sup>dim</sup>	half-maximum inhibitory concentration in the dimerization assay
GR	half-maximum inhibitory concentration in the oxidoreductase activity assay
IC <sub>50</sub> <sup>GR</sup>	half-maximum inhibitory concentration in the dimerization assay
hGR	human glutathione disulfide reductase
LiTryR	<i>Leishmania infantum</i> trypanothione disulfide reductase
PAINS	pan-assay interference compounds
PI	propidium iodide
SI	selectivity index
TbTryR	<i>Trypanosoma brucei</i> trypanothione disulfide reductase
TcTryR	<i>Trypanosoma cruzi</i> trypanothione disulfide reductase
TcoTryR	<i>Trypanosoma congolense</i> trypanothione disulfide reductase
TNB	2-nitro-5-thiobenzoic acid
Try/TryR	trypanothione/trypanothione reductase
TS <sub>2</sub>	trypanothione disulfide
T(SH) <sub>2</sub>	reduced trypanothione
VL,	visceral leishmaniasis

stages: promastigotes, the extracellular form in the female sandflies, and amastigotes, the intracellular form in the vertebrate hosts [6]. Inside the parasitophorous vacuole of host macrophages, the amastigotes are exposed to strong oxidative conditions such as the oxidative burst caused by macrophage activation. Low-molecular mass thiols and redox-regulating proteins such as the trypanothione/trypanothione disulfide reductase (T(SH)<sub>2</sub>/TryR) pair play an essential role in parasite survival under these highly stressing conditions. This T(SH)<sub>2</sub>/TryR system replaces the glutathione/glutathione disulfide reductase (GSH/GR) couple present in the hosts [7]. T(SH)<sub>2</sub> delivers electrons, directly or through the parasite thioredoxin-like tryparedoxins, to essential biochemical processes such as nuclear DNA replication [8], initiation of kinetoplast replication [9], and detoxification of metal-containing drugs [10], hydroperoxides [11], and ketoaldehydes [12]. The TS<sub>2</sub> produced in these processes is recycled back to T(SH)<sub>2</sub> by TryR, a flavoenzyme that catalyzes the electron transfer from NADPH to TS<sub>2</sub> [7].

TryR is a homodimeric enzyme closely related to other FAD-cystine oxidoreductases such as GR or thioredoxin-disulfide reductase, which are absent in *Leishmania* spp. For this reason, TryR is the only connection between the redox systems based on NADPH and cellular thiols in these parasites [7]. The essential role of this enzyme in *Leishmania* was clearly established from experiments demonstrating that generation of null mutants of the *tryA* gene encoding TryR in *L. donovani* could only be accomplished upon simultaneous episomal expression of *tryA* [13]. Nonetheless, low concentrations of this enzyme seem to be sufficient for parasite survival under non-stressing conditions, as indicated by the normal growth rates observed in *L. donovani* promastigotes expressing a *trans*-dominant mutant version of the *Trypanosoma cruzi* *tryA* gene, in which TryR activity is reduced down to 15% of that of wild-type parasites [14].

The search for TryR inhibitors as a starting point for the design and

development of new leishmanicidal drugs has been a widely employed strategy [15–18] since the discovery of the T(SH)<sub>2</sub>/TryR system in the mid-1980s [19,20]. Most of the reported TryR inhibitors target a hydrophobic region located at the entrance of the TS<sub>2</sub> binding cavity called the “mepacrine binding site”. However, they usually exhibit kinetic inhibition constants (*K<sub>i</sub>*) in the low micromolar range and low efficacies as leishmanicidal [17,21–23]. Thus, molecules targeting other binding sites in TryR have been alternatively sought and new compounds with different inhibition mechanisms have been discovered [17,24]. For some years now, our research group has been focused on the design of *L. infantum* TryR (*LiTryR*) inhibitors targeting the enzyme’s dimer interface. These inhibitors are expected to displace the equilibrium from the homodimeric (active) to the monomeric (inactive) form of *LiTryR* [25–27].

We have previously reported the dimer disruption ability of different helical peptides that mimic the pair of parallel α-helices (residues 435–447 and 435'-447') at the core of the *LiTryR* dimer interface [25]. In an attempt to obtain small molecules endowed with drug-like pharmacokinetic properties, we have recently reported a new 1,2,3-triazole-phenyl-thiazole chemotype as a novel class of *LiTryR* dimer disruptor with leishmanicidal activity [27]. As already described for peptide P4 [26], 1,2,3-triazole-based compounds with the ability to disrupt the *LiTryR* homodimer behave as noncompetitive, slow-binding inhibitors with a two-step binding mechanism [27].

The chemical structure of the most representative triazole-based compounds of general formula I is depicted in Fig. 1. Structure-activity relationship (SAR) studies revealed that lipophilic substituents at R<sub>3</sub> of mono- and disubstituted thiazole analogues significantly enhanced the disruption capacity of the enzyme in comparison with the prototype 1a. Thus, compounds 1b, 1c and 1e represented the most potent dimerization inhibitors of all the series studied. Informed by molecular modeling studies and structure-activity relationships, the central cavity at the interface domain of *LiTryR* was proposed as the putative binding site for these compounds [27].

Regarding their leishmanicidal activity, 1,2,3-triazole-based compounds exhibited potent antileishmanial activity against the axenic forms of *Leishmania* parasites. Nevertheless, they were moderately active against *L. infantum* intracellular amastigotes and showed high cytotoxicity [27]. Further improvement of these two properties was still warranted to get close to the expected values for potent and selective leishmanicidal molecules.

It has been reported that 1,2,3-triazoles can be easily *N*-alkylated with alkyl halides, tosylates or triflates to provide 3-*N*-alkyl-1,2,3-triazolium salts. This transformation usually tolerates a wide variety of functional groups, occurs in high yields, and generally provides regioselectivity towards the 3-alkyl triazolium salts [28]. This class of organic salts has been prepared for multipurpose applications, mainly in the fields of ionic liquids, organocatalysis, mesoionic carbenes, or as components of supramolecular assemblies [29,30]. Yet, the strategy of exploiting their biological activity has been little explored. Only in recent years have a few examples of 1,2,3-triazolium salts shown promising results as anticancer [31–33], antimicrobial [34], antifungal [35], or antileishmanial agents [36,37].

In view of the above, preparing quaternized analogues derived from our 1,2,3-triazole-phenyl-thiazole anti-leishmanial compounds I seemed like an attractive and worth-exploring possibility. The unique properties and novelty of the triazolium-phenyl-thiazol chemotype endowed with an extra positive charge and altered hydrogen bonding potential prompted us to synthesize and screen a small library of compounds of general formula II (Fig. 1) against *LiTryR* and evaluate their antileishmanial activity.

We herein describe the significant impact of the *N*-alkylation of the triazole-based inhibitors on (i) the enzymatic and *in cellulo* activity of *LiTryR*, and (ii) crucial physicochemical properties such as water solubility. Rewardingly, replacement of the 1,2,3-triazole moiety with the corresponding 1,2,3-triazolium salt led to the discovery of a new family

of potent *LiTryR* competitive inhibitors while several derivatives bearing a biphenylethyl substituent at  $R_3$  maintained the strong *LiTryR* dimer disrupting abilities of their parent triazoles. *In vitro* kinetic characterization, X-ray crystallography, and computational studies have allowed us to identify two different binding sites for the compounds at the enzyme. In general, the triazolium salt analogues that were highly active as disruptors of the *LiTryR* dimer significantly improved both potency and selectivity against intracellular amastigotes with  $SI > 10$ . Importantly, the dimerization disruptor **4c** significantly reduces the content of low-molecular-weight thiols in the parasites, a finding that can be taken as strong evidence of inhibition of the endogenous *LiTryR* activity. Thus, the triazolium salt-based dimer disruptors of *LiTryR* may become promising and innovative candidates for further development as a new generation of antileishmanial agents.

## 2. Results and discussion

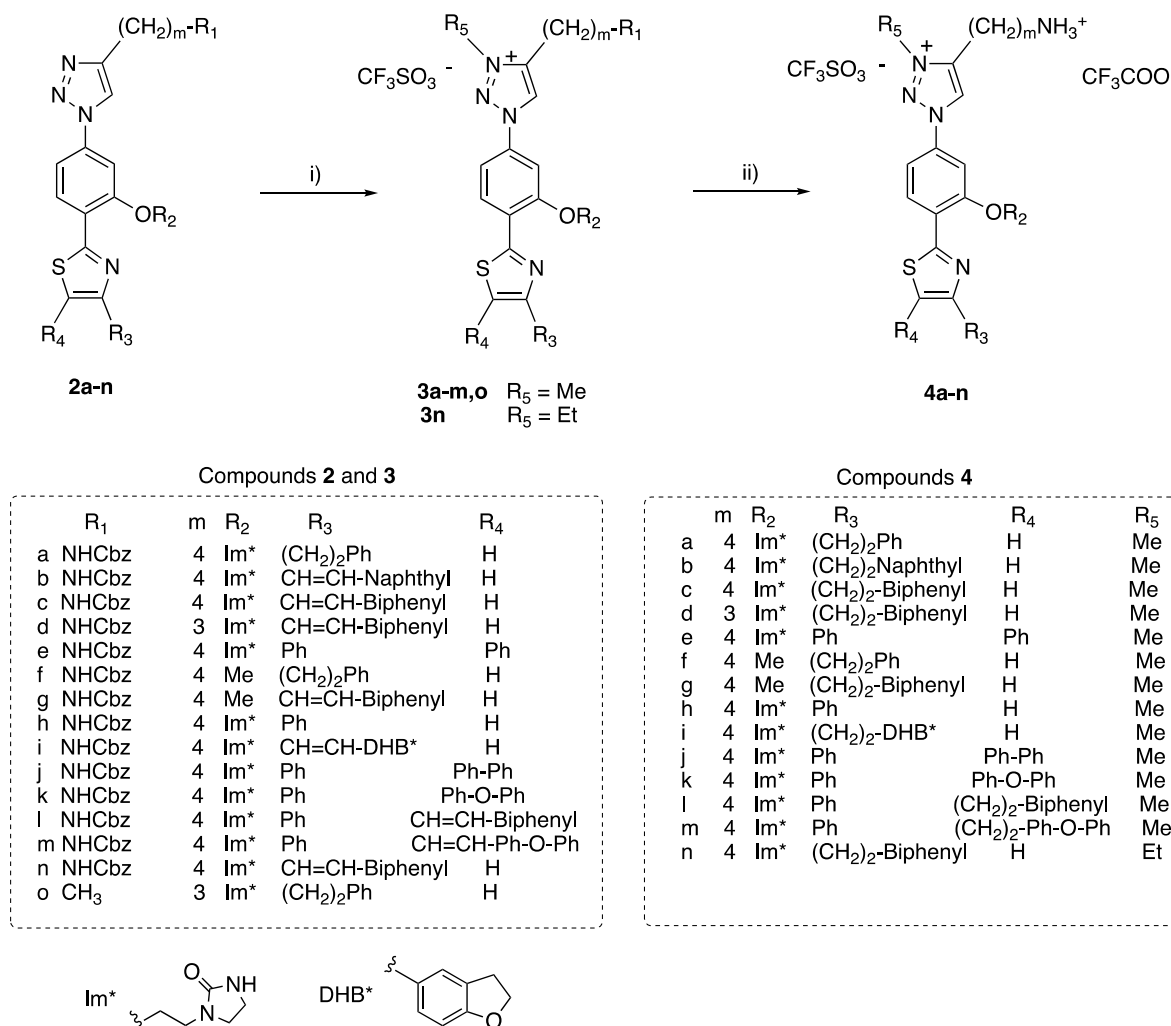
### 2.1. Chemistry

The synthesis of the new triazolium salts **II** (Scheme 1) involves the *N*-alkylation of the triazole ring of previously described protected triazole-phenyl-thiazole precursors **I** [27] followed by removal of the protecting groups to give the final deprotected target compounds. Initial attempts of alkylation of *N*-Cbz-protected triazole compound **2a** with methyl iodide (2 eq) in dry acetonitrile at 80 °C for 24 h were

unsuccessful and only starting material was recovered. However, the use of an excess of reagent (10 eq) and extended reaction times (48 h) [38] afforded the regioisomer 3-*N*-methylated 1,2,3-triazolium salt **3a** in 35% yield together with unreacted starting material and minor dimethylated products identified by HPLC-MS that were not isolated in the chromatographic purification.

Compound **3a** (isolated as the hydroiodide salt) was fully characterized by mono- and bidimensional  $^1\text{H}$  and  $^{13}\text{C}$  NMR experiments. The  $^1\text{H}$  NMR spectrum of **3a** corroborated the quaternization reaction by showing a large downfield shift of the triazolium proton H-5 in **3a** (from 6.86 ppm in the triazole **2a** to 9.24 ppm) and the appearance of the new 3-*N*-methyl proton at 4.42 ppm (in  $\text{CD}_3\text{OD}$ ). Although the nature of the alkylating agent and the steric hindrance of the triazole positions play a fundamental role in the selectivity of the reaction, the functionalization at 3-*N* is the most favorable [28]. In line with previous examples of 1,2,3-triazole quaternization, 1D-NOESY and 2D-HMBC NMR data unequivocally identified the structure of compound **3a** as the 3-*N*-methyl triazolium salt (see Fig. S1 in the Supplementary Material).

We next performed an optimization study of the *N*-alkylation reaction of **2a** with Meerwein's salt ( $\text{Me}_3\text{OBF}_4$ ) [39] or methyl triflate ( $\text{MeOTf}$ ) [40] as alkylating reagents in dry  $\text{CH}_2\text{Cl}_2$  at room temperature by monitoring the reaction using HPLC. Higher conversions, reduced amounts of dimethylated compounds and much shorter reaction times were observed by HPLC (see Table S1 and Fig. S2 in the Supplementary Material). Optimal reaction conditions were obtained by treatment of **2a**



**Scheme 1.** Synthesis of target triazolium salts compounds **3o** and **4a-n** by *N*-alkylation and deprotection of triazole parent compounds **2a-n**. *Reagents and conditions:* i)  $\text{R}_5\text{OTf}$ ,  $\text{CH}_2\text{Cl}_2$  anh, rt, 15 min; ii)  $\text{H}_2$  Pd/C 10%, TFA, THF/MeOH, 1:1, 2h.

with MeOTf (1 eq) in dry CH<sub>2</sub>Cl<sub>2</sub> at room temperature for 15 min which allowed access to the trifluoromethanesulfonate salt **3a** in 85% yield. Under the optimized alkylation conditions, other triazole-protected compounds (with a variety of substituents at R<sub>1</sub>-R<sub>4</sub>) were reacted with MeOTf affording the 1,2,3-triazolium salts **3b-m,o** in good yields (70–85%) (Scheme 1). In addition, the use of ethyl triflate as the alkylating reagent afforded the 3-*N*-ethylated 1,2,3-triazolium salt derivative **3n** although in a lower yield (45%). Finally, treatment of the *N*-Cbz protected triazolium salts **3a-m,o** and **3n** with H<sub>2</sub>, Pd/C in THF/MeOH mixture in the presence of trifluoroacetate (TFA) furnished the target deprotected triazolium compounds **4a-n**, which were isolated as TFA and triflate disalts in low to moderate yields after reversed-phase chromatographic purification.

New triazolium salts **9a** and **9b** modified at R<sub>2</sub> with an ethyl or methyl piperidinium moiety (Scheme 2) were next prepared in attempts to improve the binding affinity. The design of these compounds was based on structural information gathered from the crystal structure of LiTryR in complex with triazolium salt **4a** (see rationale and discussion in the X-ray structural section). The preparation of the corresponding triazole-phenyl-thiazole precursors following our reported procedure [27] would involve the introduction of the R<sub>2</sub> substituent at the first step of the synthetic route. We decided to explore an alternative and more efficient late-stage functionalization approach to introduce the R<sub>2</sub> substituents at later steps of the synthesis from the key phenol intermediate **5** (Scheme 2). The triazole-phenyl-thiazole analogue **2f** with a methoxy group at R<sub>2</sub> was used as the starting compound. Deprotection of the methoxy group was first attempted using reported conditions [41]. Thus, treatment of **2f** with 3 equiv. of a solution of BBr<sub>3</sub> in dry CH<sub>2</sub>Cl<sub>2</sub> (slowly added at –78 °C) stirring the reaction at room temperature for 20 h, followed by quenching with water and methanol for 1 h, gave the desired phenol **5** in very low yields (8%) together with unreacted starting material. An optimization study of this reaction varying the

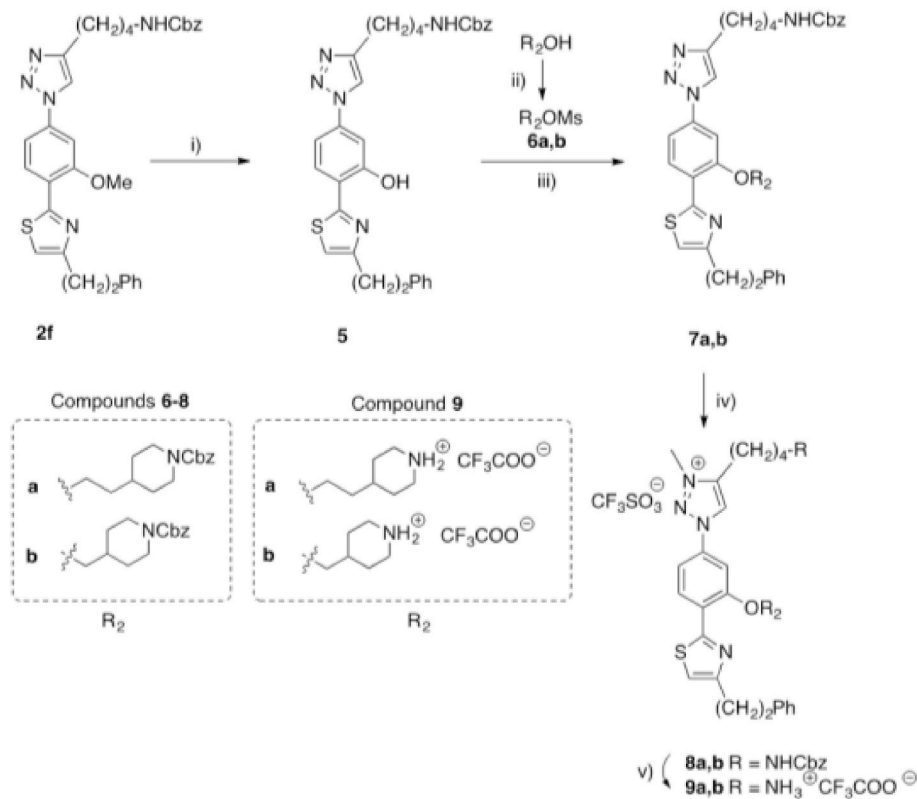
number of equivalents of BBr<sub>3</sub>, the temperature, and the reaction and quenching times was performed (see Table S2 in the Supplementary Material). Optimal reaction conditions involved the use of an increased number of equivalents of the Lewis acid (sequential addition of 10 + 10 eq), shorter reaction times keeping the temperature at –78 °C to avoid the *N*-Cbz deprotection (from 20 h to 4 h) and extending quenching times (from 1 h to 12 h) to efficiently break the observed formation of complexes of the Lewis acid with the compounds (probably with the triazole's N atoms). Under these optimal conditions, the yield of the desired phenol intermediate **5** was significantly increased from 8% to 62%.

Etherification of phenol compound **5** was next achieved by means of an S<sub>N</sub>2 reaction with methanesulfonates bearing the appropriate R<sub>2</sub> substituents (Scheme 2). Thus, activation of the commercially available *N*-protected primary alcohols with mesyl chloride in the presence of DMAP and NEt<sub>3</sub> in dry DMF afforded the methanesulfonates **6a** [42] and **6b** [43] in good yields. Subsequent treatment of these compounds with phenol **5** in the presence of K<sub>2</sub>CO<sub>3</sub> in dry DMF at 50–80 °C gave the *N*-protected triazole-phenyl-thiazole intermediates **7a** and **7b** in 66% and 97% yields, respectively.

Further alkylation of the triazole moiety with MeOTf (using the optimized conditions mentioned above) followed by 10% Pd/C-catalyzed hydrogenolysis yielded the new deprotected triazolium salts **9a** and **9b** modified at R<sub>2</sub> isolated as ditrifluoroacetate and monotriflate trisalts in moderate yields after reversed-phase chromatographic purification (Scheme 2).

### 2.1.1. Experimental water solubility

The aqueous thermodynamic solubilities (S<sub>exp</sub>) of the most representative parent triazole- and triazolium salt-based compounds were determined at 25 °C after 24 h. It was expected that the quaternization of the 1,2,3-triazoles could help improve water solubility by the



**Scheme 2.** Synthesis of the newly designed triazolium salts compounds **9a,b** modified at R<sub>2</sub>. *Reagents and conditions:* i) a) BBr<sub>3</sub> 10 + 10 eq, CH<sub>2</sub>Cl<sub>2</sub> anh, –78 °C, 4h, b) MeOH, H<sub>2</sub>O, rt 12 h; ii) MeSO<sub>2</sub>Cl, DMAP, NEt<sub>3</sub>, CH<sub>2</sub>Cl<sub>2</sub> anh, 0 °C – rt, 12 h; iii) **6a,b**, K<sub>2</sub>CO<sub>3</sub>, DMF anh, 50 °C – 80 °C, 2 h; iv) MeOSO<sub>3</sub>CF<sub>3</sub>, CH<sub>2</sub>Cl<sub>2</sub> anh, rt, 15 min; v) H<sub>2</sub> Pd/C 10%, TFA, THF/MeOH (1:1), 2 h.

introduction of an additional positive charge at the triazole. The  $S_{exp}$  of triazolium salts **4a-d** (>15.9, 23.5, 12.4, 21.6 mg/mL, respectively) was indeed much higher than that of their triazole counterparts **1a-d** (6.4, 2.1, 0.2, 2.8 mg/mL, respectively), even by 1 or 2 order(s) of magnitude (cf. **4b,d** or **4c** vs **1b,d** or **1c**). According to the solubility criteria of the United States Pharmacopoeia (USP30/NF25), all compounds can be classified as very soluble since less than 1 part solvent (water) is required to dissolve 1 part solute.

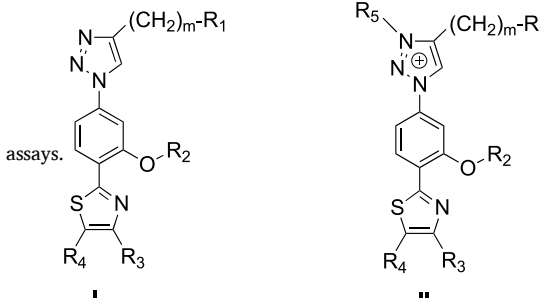
## 2.2. Biological evaluation

### 2.2.1. Enzymatic assays

The 1,2,3-triazolium salt analogues of our recently described 1,2,3-triazole-phenyl-thiazoles were evaluated for their ability to inhibit *LiTryR* oxidoreductase activity and to alter the homodimeric state of this enzyme. The prototype peptide **P4** as well as the 1,2,3-triazole-phenyl-thiazoles **1a-e** were used as reference molecules in these SAR studies [27]. All the 1,2,3-triazolium salts were first tested in preliminary screening assays at 75  $\mu$ M (maximum assayed concentration). Compounds displaying more than 50% of inhibition either in the oxidoreductase activity or in the dimerization assay were selected for determination of their half-maximal inhibitory concentrations (Table 1).

**Table 1**

$IC_{50} \pm SE$  values for triazolium salts **3o**, **4a-n** and **9a,b** in the *LiTryR* oxidoreductase activity and in the *LiTryR* monomer displacement



Compound	Series	R <sub>1</sub>	m	R <sub>2</sub>	R <sub>3</sub>	R <sub>4</sub>	R <sub>5</sub>	$IC_{50}^{act}$ ( $\mu$ M) <sup>b</sup>	$IC_{50}^{dim}$ ( $\mu$ M) <sup>c</sup>
Peptide <b>P4</b> <sup>a</sup>	–	–	–	–	–	–	–	1.5 $\pm$ 0.2	7.0 $\pm$ 0.6
Representative parent triazoles									
<b>1a</b> <sup>a</sup>	I	NH <sub>3</sub> <sup>+</sup>	4	(CH <sub>2</sub> ) <sub>2</sub> Im*	(CH <sub>2</sub> ) <sub>2</sub> Ph	H	–	14.6 $\pm$ 1.0	38.1 $\pm$ 1.2
<b>1b</b> <sup>a</sup>	I	NH <sub>3</sub> <sup>+</sup>	4	(CH <sub>2</sub> ) <sub>2</sub> Im*	(CH <sub>2</sub> ) <sub>2</sub> Naphthyl	H	–	5.9 $\pm$ 1.1	7.1 $\pm$ 0.6
<b>1c</b> <sup>a</sup>	I	NH <sub>3</sub> <sup>+</sup>	4	(CH <sub>2</sub> ) <sub>2</sub> Im*	(CH <sub>2</sub> ) <sub>2</sub> Biphenyl	H	–	10.9 $\pm$ 1.8	4.8 $\pm$ 0.6
<b>1d</b> <sup>a</sup>	I	NH <sub>3</sub> <sup>+</sup>	3	(CH <sub>2</sub> ) <sub>2</sub> Im*	(CH <sub>2</sub> ) <sub>2</sub> Biphenyl	H	–	19.7 $\pm$ 3.8	10.8 $\pm$ 0.1
<b>1e</b> <sup>a</sup>	I	NH <sub>3</sub> <sup>+</sup>	4	(CH <sub>2</sub> ) <sub>2</sub> Im*	Ph	Ph	–	4.3 $\pm$ 1.0	7.1 $\pm$ 1.7
Triazolium salt analogues									
<b>4a</b>	II	NH <sub>3</sub> <sup>+</sup>	4	(CH <sub>2</sub> ) <sub>2</sub> Im*	(CH <sub>2</sub> ) <sub>2</sub> Ph	H	Me	9.4 $\pm$ 1.6	>75
<b>4b</b>	II	NH <sub>3</sub> <sup>+</sup>	4	(CH <sub>2</sub> ) <sub>2</sub> Im*	(CH <sub>2</sub> ) <sub>2</sub> Naphthyl	H	Me	2.7 $\pm$ 0.1	>75 (29%) <sup>d</sup>
<b>4c</b>	II	NH <sub>3</sub> <sup>+</sup>	4	(CH <sub>2</sub> ) <sub>2</sub> Im*	(CH <sub>2</sub> ) <sub>2</sub> Biphenyl	H	Me	5.2 $\pm$ 0.8	10.3 $\pm$ 1.6
<b>4d</b>	II	NH <sub>3</sub> <sup>+</sup>	3	(CH <sub>2</sub> ) <sub>2</sub> Im*	(CH <sub>2</sub> ) <sub>2</sub> Biphenyl	H	Me	7.0 $\pm$ 0.6	45.4 $\pm$ 2.2
<b>4e</b>	II	NH <sub>3</sub> <sup>+</sup>	4	(CH <sub>2</sub> ) <sub>2</sub> Im*	Ph	Ph	Me	3.9 $\pm$ 0.3	>75
Modifications at R <sub>1</sub> -R <sub>5</sub>									
<b>3o</b>	II	CH <sub>3</sub>	3	(CH <sub>2</sub> ) <sub>2</sub> Im*	(CH <sub>2</sub> ) <sub>2</sub> Ph	H	Me	42.0 $\pm$ 4.2	>75
<b>4f</b>	II	NH <sub>3</sub> <sup>+</sup>	4	OMe	(CH <sub>2</sub> ) <sub>2</sub> Ph	H	Me	18.3 $\pm$ 2.3	>75
<b>4g</b>	II	NH <sub>3</sub> <sup>+</sup>	4	OMe	(CH <sub>2</sub> ) <sub>2</sub> Biphenyl	H	Me	5.5 $\pm$ 0.7	>75
<b>4h</b>	II	NH <sub>3</sub> <sup>+</sup>	4	(CH <sub>2</sub> ) <sub>2</sub> Im*	Ph	H	Me	20.3 $\pm$ 1.2	>75
<b>4i</b>	II	NH <sub>3</sub> <sup>+</sup>	4	(CH <sub>2</sub> ) <sub>2</sub> Im*	(CH <sub>2</sub> ) <sub>2</sub> DHB*	H	Me	5.4 $\pm$ 0.2	>75
<b>4j</b>	II	NH <sub>3</sub> <sup>+</sup>	4	(CH <sub>2</sub> ) <sub>2</sub> Im*	Ph-Ph	Ph	Me	4.0 $\pm$ 0.2	>75
<b>4k</b>	II	NH <sub>3</sub> <sup>+</sup>	4	(CH <sub>2</sub> ) <sub>2</sub> Im*	Ph-OPh	Ph	Me	4.2 $\pm$ 0.2	>75
<b>4l</b>	II	NH <sub>3</sub> <sup>+</sup>	4	(CH <sub>2</sub> ) <sub>2</sub> Im*	(CH <sub>2</sub> ) <sub>2</sub> Biphenyl	Ph	Me	6.8 $\pm$ 1.2	>75
<b>4m</b>	II	NH <sub>3</sub> <sup>+</sup>	4	(CH <sub>2</sub> ) <sub>2</sub> Im*	(CH <sub>2</sub> ) <sub>2</sub> Ph-OPh	Ph	Me	7.8 $\pm$ 0.9	>75
<b>4n</b>	II	NH <sub>3</sub> <sup>+</sup>	4	(CH <sub>2</sub> ) <sub>2</sub> Im*	(CH <sub>2</sub> ) <sub>2</sub> Biphenyl	H	Et	3.9 $\pm$ 0.6	56.9 $\pm$ 2.5
Modifications at R <sub>2</sub> (Scheme 2)									
<b>9a</b>	II	NH <sub>3</sub> <sup>+</sup>	4	(CH <sub>2</sub> ) <sub>2</sub> Pip*	(CH <sub>2</sub> ) <sub>2</sub> Ph	H	Me	2.2 $\pm$ 0.4	>75
<b>9b</b>	II	NH <sub>3</sub> <sup>+</sup>	4	CH <sub>2</sub> Pip*	(CH <sub>2</sub> ) <sub>2</sub> Ph	H	Me	2.1 $\pm$ 0.3	>75

<sup>a</sup> Data from peptide **P4** and the parent triazole compounds **1a-e** are also included for comparison reasons [27].

<sup>b</sup> *LiTryR* oxidoreductase activity assay.

<sup>c</sup> Dimer quantitation assay (ELISA). Enzymatic activity >75 indicates that the  $IC_{50}$  value is higher than 75  $\mu$ M (maximum assayed). Results are representative of three independent experiments.

<sup>d</sup> Percentage of inhibition observed at 75  $\mu$ M. Im\* = imidazolidinone, DHB\* = dihydrobenzofuranyl, Pip\* = piperidine.

shortening the four-methylene linker by one carbon atom decreased the dimerization disruption capacity >4-fold (**4c** vs **4d**) (Table 1).

Regarding the R<sub>2</sub> substituent, replacement of the imidazolidinone ethyl group by a methyl group annihilated the capacity to disrupt the *LiTryR* homodimer (**4g** vs **4c**), although the ability to inhibit the oxidoreductase activity of the enzyme was retained (**4f,g** vs **4a,c**) (Table 1). Substitution of a piperidine moiety for the imidazolidinone at R<sub>2</sub> increased their inhibitory activity up to >4-fold (**4a** vs **9a,b**) (Table 1).

In terms of the different modifications explored at the R<sub>3</sub> substituent (located at the 4-position of the thiazole ring), the presence of bulky and hydrophobic poly-(hetero)aromatic groups is a common feature of the triazolium salt derivatives showing the lowest IC<sub>50</sub><sup>act</sup> values (**4b-d,g,i,n**) (Table 1). Disubstituted triazolium salts bearing combinations of (poly) aromatic groups at R<sub>3</sub> and a phenyl group as an additional R<sub>4</sub> substituent at position 5 of the thiazole ring also exhibited a potent inhibition of *LiTryR* activity (**4e,j-m**) (Table 1). In particular, when a phenyl, a biphenyl or a phenyloxyphenyl group is directly attached to the R<sub>3</sub> substituent of these disubstituted compounds, IC<sub>50</sub><sup>act</sup> values of about ~4 μM are obtained (**4e,j,k**) (Table 1). On the other hand, linkage of polyaromatic groups at R<sub>3</sub> through an ethylene spacer leads to a slight loss of inhibitory activity for the disubstituted triazolium salts (**4j,k** vs **4l,m**) (Table 1).

Substitution of an ethyl group for the methyl at R<sub>5</sub> did not have any relevant effect on the oxidoreductase activity of *LiTryR* (**4c** vs **4n**) although a 6-fold reduction of potency was observed in the dimerization assay (Table 1).

In general, 1,2,3-triazolium salts were more potent inhibitors of *LiTryR* oxidoreductase activity than their triazole counterparts. However, contrary to what was observed in the original 1,2,3-triazole-phenyl-thiazoles, most of their triazolium salt analogues could not interfere with *LiTryR* dimerization. Indeed, the presence of amino alkyl, imidazolidinone ethyl, biphenylethyl and alkyl groups at R<sub>1</sub>, R<sub>2</sub>, R<sub>3</sub> and R<sub>5</sub> substituents, respectively, together with the absence of a phenyl group at R<sub>4</sub>, is as an absolute requirement for retaining the capacity to disrupt the *LiTryR* homodimer (**4c,d,n**).

## 2.2.2. Inhibitory activity on TryR Enzymes from other members of the trypanosomatidae Family and Selectivity against human glutathione reductase

Representative compounds **4a-c** were studied as inhibitors of TryRs from several pathogenic trypanosomatids, namely *Trypanosoma brucei* (*TbTryR*), *Trypanosoma cruzi* (*TcTryR*) and *Trypanosoma congolense* (*TcoTryR*), the causative agents of sleeping sickness, Chagas disease and nagana, respectively. In addition, to gain insight into the selectivity of the prioritized compounds **4a-c** for TryR, their ability to inhibit the oxidoreductase activity of the closely related GR from the human host (hGR) was also tested. All the assays were performed using enzyme concentrations that generated similar maximal velocities of reaction and a concentration of 50 μM of the respective oxidized disulfide substrates. This substrate concentration is above the K<sub>m</sub> values described for TS<sub>2</sub> in trypanosomatid TryRs and below that observed for oxidized glutathione in hGR. As shown in Table 2, it is worth noting that none of the triazolium salts inhibited the oxidoreductase activity of hGR at the maximum concentration assayed. The IC<sub>50</sub><sup>act</sup> values of the triazolium salt **4a** varied from 18.7 μM in *TcoTryR* to about ~27 μM in *LiTryR* and

**Table 2**

IC<sub>50</sub> ± SE values (μM) for selected triazolium salts compounds **4a-c** in the oxidoreductase activity assay of TryRs from different pathogenic trypanosomatids and hGR.

Compound	<i>LiTryR</i>	<i>TbTryR</i>	<i>TcTryR</i>	<i>TcoTryR</i>	hGR
<b>4a</b>	27.0 ± 0.9	26.9 ± 2.5	48.5 ± 4.9	18.7 ± 0.8	>75
<b>4b</b>	2.9 ± 0.1	5.1 ± 0.2	9.2 ± 0.5	4.2 ± 0.3	>75
<b>4c</b>	3.1 ± 0.3	4.9 ± 1.3	9.2 ± 1.2	3.6 ± 0.8	>75

*TbTryR*, and 48.5 μM in *TcTryR*. Remarkably, compared to *LiTryR*, the potency of the dimer disruptors **4b,c** was slightly reduced in *TcoTryR* and decreased only 1.5- to 2-fold in *TbTryR*, and ~3-fold in *TcTryR* (Table 2).

## 2.2.3. Competitive inhibition of *LiTryR* by non-disruptive triazolium salts

As already discussed, most of the triazolium salts did not interfere with *LiTryR* dimerization. Similarly to what is found for the classical competitive inhibitor mepacrine, the reaction rates observed in the presence of these compounds are almost constant until Ellman's reagent (which regenerates the TS<sub>2</sub> substrate) is consumed. Compound **4a**, which bears the most representative substituents of this series of triazolium salts, was selected for further kinetic characterization. The inhibition modality of this compound was determined by measuring the initial velocities of the different reactions performed at different concentrations of TS<sub>2</sub> and **4a**. Our data nicely fit to the classic linear competitive model in which an inhibitor (I) binds exclusively to the free enzyme (E) generating a binary and dead-end enzyme-inhibitor complex (EI) (Fig. 2). In this model, both substrate and inhibitor compete for the pool of free enzyme molecules because binding proceeds in a mutually exclusive fashion [44,45]. The inhibition constant (K<sub>i</sub>) for the dissociation of the binary EI complex formed by the triazolium salt **4a** and the TS<sub>2</sub>-depleted *LiTryR* yielded a value of 7.3 ± 0.9 μM. As shown in Fig. 2B, a nest of lines intersecting at the same value on the y-axis is observed in the Lineweaver-Burk double reciprocal plot. This distinctive signature of competitive inhibitors is indicative of a constant V<sub>max</sub> value at different inhibitor concentrations [44,45]. A congruent K<sub>D</sub> value of 1 μM was obtained for **4a** when analyzed by surface plasmon resonance (see Fig. S13 in the Supplementary Material).

## 2.2.4. Binding mode of non-disruptive triazolium salts

Soaking of *LiTryR* crystals with **4a** permitted the atomic structure elucidation of the *LiTryR-4a* complex at 2.5 Å resolution (Table 3). The asymmetric unit contains a monomer of *LiTryR* and one **4a** molecule bound to the enzyme's active site, hence the functional dimer is formed with the concurrence of a symmetry-related molecule (Fig. 3A).

A continuous, well-defined electron density is observed for **4a** close to the catalytic cysteine residues (C52 and C57) and the FAD prosthetic group (Fig. 3B). Inhibitor binding relies on crucial interactions with residues making up the so-called "polyamine-binding site" (Glu18, Trp21 and Tyr110) which are involved in TS<sub>2</sub> anchoring [46]. This binding location has also been described for other *LiTryR* inhibitors such as quinacrine derivatives [47], cyclohexylpyrrolidines [23,48], and pyrrolopyrimidines [49]. Both the R<sub>2</sub> substituent and the thiazole ring of **4a** play an important role in ligand stabilization (Fig. 3B). Thus, stacking interactions are made by (i) the linker in R<sub>2</sub> bearing the imidazolidinone at the end and Trp21, (ii) the central phenyl ring and Met113, and (iii) the thiazole ring and Tyr110. In addition, hydrogen bonds are formed between the Glu18 carboxylate and the NH group of the heterocycle in R<sub>2</sub>, and also between the hydroxyl group of Ser109 and the thiazole ring nitrogen. Other interactions involve (iv) Asp116, which electrostatically engages the triazole ring of the scaffold, (v) the butylamine in R<sub>1</sub> that is oriented towards negatively charged residues lining the outer part of the active site, and (vi) the phenylethyl R<sub>3</sub> substituent, which faces a hydrophobic pocket inside the cavity lined by Val53, Val102, Val103, and Ile106 (Fig. 3B).

Informed by this *LiTryR:4a* complex, a structure-based approach led to the design and synthesis of the piperidine derivative **9a** with a view to strengthening the interaction between the R<sub>2</sub> substituent and Glu18 by means of an ionic hydrogen bond, as well as the π-cation interaction with the indole ring of Trp21 (Fig. 3B). As expected, enzyme inhibition by the new triazolium **9a** was significantly enhanced (about ~4-fold) and this piperidine derivative currently represents one of the most potent *LiTryR* oxidoreductase inhibitors of the entire series, with an IC<sub>50</sub><sup>act</sup> value of 2.2 μM similar to that of the original prototype peptide **P4**.

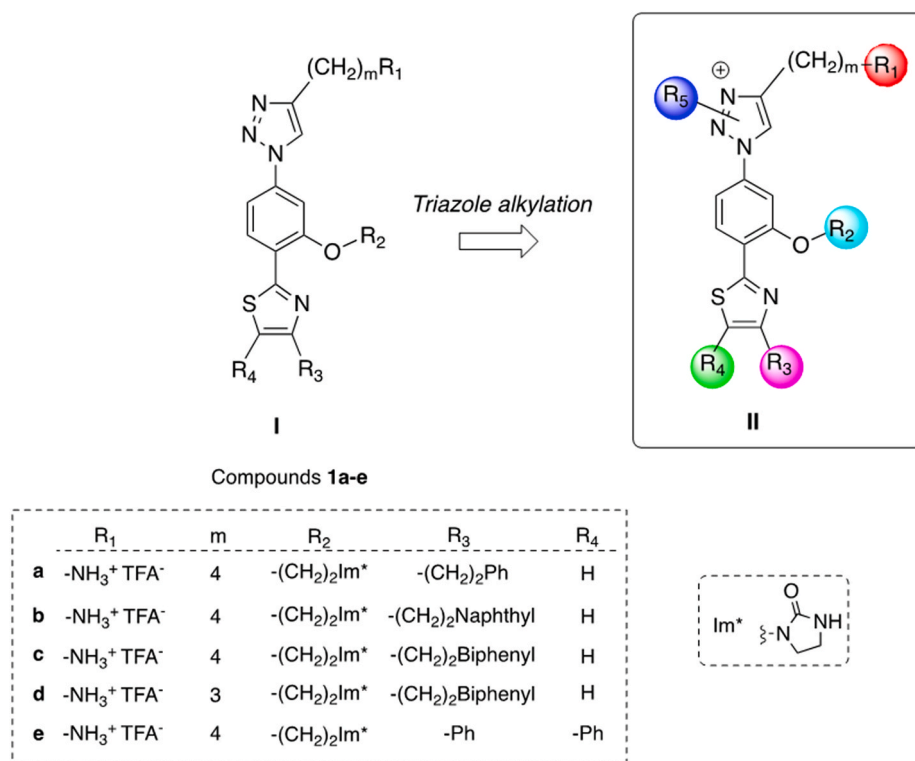


**Fig. 1.** Newly designed triazolium salts chemotype **II** from in-house triazole-phenyl-thiazole scaffold **I**. Chemical structure of the most representative parent triazole compounds **1a-e**.

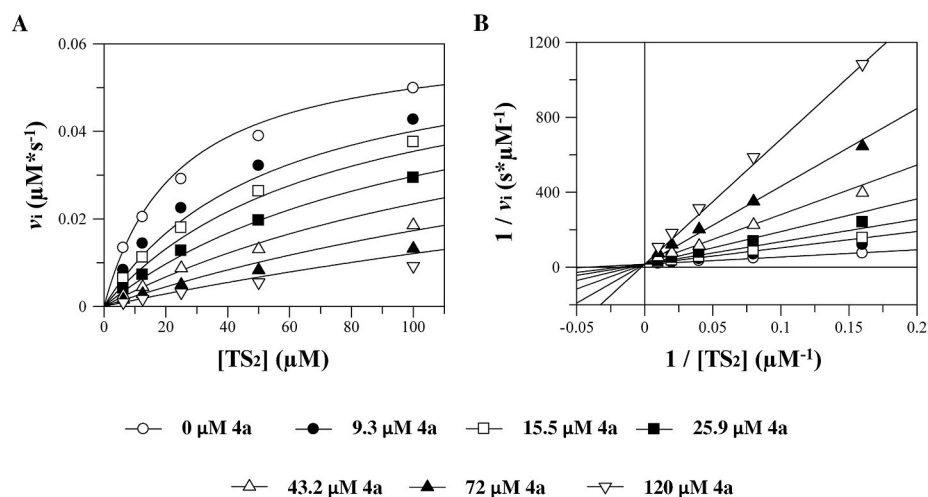


**Fig. 2.** Competitive inhibition of *LiTryR* by the triazolium salt **4a**. (A) Plot of the initial velocities ( $v_i$ ) as a function of oxidized trypanothione disulfide (TS<sub>2</sub>) at seven different concentrations of compound **4a**. 2-nitro-5-thiobenzoic acid (TNB) production was monitored by the absorbance at 412 nm. Curves were fitted using Equation 1. (B) Double-reciprocal plot. Data are from results obtained in a representative assay from three independent experiments.

The crystal structure of *LiTryR* in complex with **9a**, solved at 3 Å resolution after soaking (Table 3), showed **9a** located and positioned in the enzyme's polyamine-binding site similarly to **4a** (Fig. 4A). In both cases, the *LiTryR* structure changes only slightly upon binding of **4a** or **9a** (rmsd of 0.19 Å after superposition of all C $\alpha$  atoms) and mostly involves reorientation of several amino acid side chains. As anticipated, the R<sub>2</sub> linker stacks on Trp21 and the distal piperidine ring nitrogen electrostatically binds to Glu18, whilst other interactions involving the common scaffold remain constant, except for a slight rotation about the central phenyl ring (Fig. 4B) brought about by distinct adaptation to the binding pocket.

Using this crystallographic information, unrestrained molecular

dynamics (MD) simulations were run for the complexes of *LiTryR* with **4a** and **9a** in an attempt to represent the ensemble of structures present in solution and to get estimates of the corresponding ligand binding energies. As anticipated from the increased positive charge at the R<sub>2</sub> substituent, the interaction with Glu18 was stronger for **9a** relative to **4a** (Fig. 5), in good accord with the 4-fold increase in inhibitory activity (Table 1). Furthermore, the calculations revealed the relative importance of the electrostatic interaction between the negatively charged carboxylate of Asp116 (Fig. 5) and the positively charged triazolium as well as the R<sub>1</sub> substituent in both ligands.

**Table 3**  
Crystallographic data collection and refinement statistics.

Parameters	LiTryR-4a Complex	LiTryR-9a Complex
Data collection		
Space group	P 4 <sub>1</sub> 2 <sub>1</sub> 2	P 4 <sub>1</sub> 2 <sub>1</sub> 2
Cell dimensions		
a, b, c (Å)	103.50, 103.50, 192.22	103.43, 103.43, 192.79
α, β, γ (°)	90, 90, 90	90, 90, 90
Wavelength (Å)	0.97929	0.979260
Resolution (Å)	73.2-(2.6–2.5)	68.4-(3.2–3.0)
Total reflections	214257 (20889)	113207 (19460)
No. unique reflections	36767 (4081)	21445 (3411)
R <sub>pim</sub>	0.042 (0.269)	0.081 (0.298)
CC <sub>1/2</sub>	0.996 (0.904)	0.965 (0.831)
I/σ(I)	9.6 (2.2)	5.6 (1.7)
Completeness (%)	99.5 (99.3)	98.9 (99.5)
Multiplicity	5.9 (5.1)	5.3 (5.7)
<b>Refinement</b>		
Resolution range (Å)	73.2–2.5	68.4–3.0
R <sub>work</sub> /R <sub>free</sub>	0.2195/0.2474	0.2149/0.2571
No. atoms		
Protein	3710	3710
Water	260	148
Ligand	161	138
Root-mean-square deviations		
Bond length (Å)	0.003	0.007
Bond angles (°)	1.2349	1.5114
Ramachandran favored/outliers (%)	100/0	99.38/0.62
Residues in AU	489	489
Average B value overall (Å <sup>2</sup> )	52.00	71.15
<b>PDB code</b>	<b>6T95</b>	<b>6T98</b>

\*Value for the highest resolution shell is shown in parenthesis.

### 2.2.5. Mixed time-dependent mechanism of LiTryR inhibition by triazolium salts dimerization disruptors

In an attempt to elucidate the inhibition mechanism of the triazolium salts endowed with dimer disruption capacity, compound **4c** showing the lowest IC<sub>50</sub><sup>dim</sup> value was selected for further kinetic characterization. As already described for other dimer disruptors of LiTryR, such as peptide **P4** [26] and 1,2,3-triazole-phenyl-thiazoles [27], the progress of the LiTryR oxidoreductase reactions in the presence of **4c** displays a curvilinear relationship on a time scale in which the progress curve of the uninhibited reaction is linear (see Figs. S3–S9 in the Supplementary Material). This behavior is typical of slow-binding inhibitors, whose distinctive hallmark is a variation of the inhibition rates over time as the steady-state equilibrium between all possible conformations of the enzyme, the inhibitor, and the enzyme-inhibitor complex(es) is slowly established [44,45,50].

Detailed observation of the reaction progress curves at fixed TS<sub>2</sub> concentrations revealed that increasing concentrations of **4c** decrease both the initial reaction rates (v<sub>i</sub>) and the final steady-state velocities (v<sub>s</sub>). This behavior points to the formation of two different enzyme-inhibitor complexes, which is a distinguishing feature of the two-step induced-fit mechanism of time-dependent inhibition (Scheme 3) [45]. This mechanism involves an initial rapid equilibrium between E and I to form an EI encounter complex, which is followed by slow inhibitor-induced isomerization of the enzyme to a higher affinity complex termed E\*I. This slow conformational transition of the enzyme gives rise to the distinctive bending of the reaction progress curve in the presence of the time-dependent inhibitor [44,45,50].

The reaction progress curves obtained in the presence of different concentrations of TS<sub>2</sub> and **4c** were fitted to Equation (1). This equation

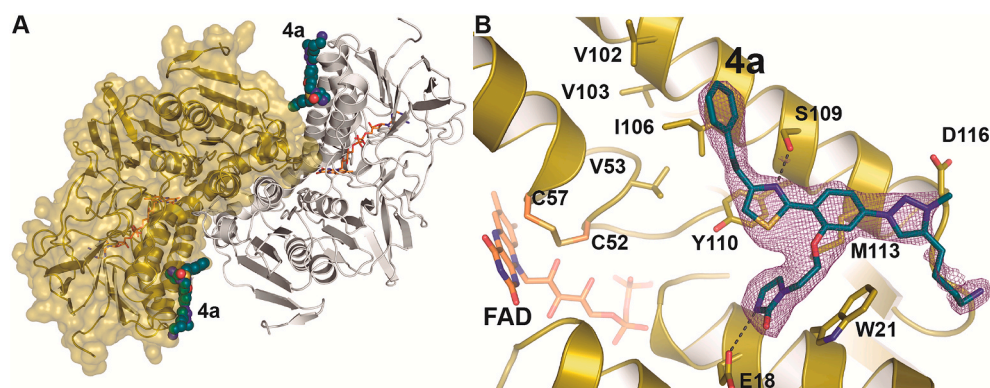


**Fig. 3.** Three-dimensional structure of LiTryR in complex with **4a**. (A) The LiTryR dimer bound to **4a** (shown as spheres). The LiTryR monomer observed in the asymmetric unit of the crystal is colored yellow and its surface displayed. The second LiTryR chain is colored white. The FAD cofactor and catalytic Cys residues are shown as orange sticks. (B) Close-up view of the binding site of **4a**. The inhibitor binds in the polyamine-binding site where its natural substrate would bind. The ligand is shown as green sticks and its corresponding 2F<sub>o</sub>-F<sub>c</sub> electron density is contoured as a purple mesh at 1σ. Relevant amino acids are depicted as capped sticks and labeled accordingly. Polar contacts represented as dashed lines.

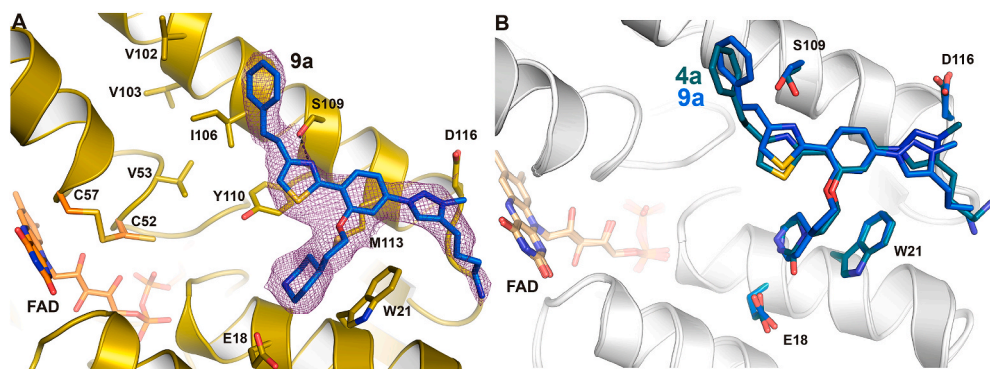


**Fig. 4.** Binding site of **9a** and comparison with **4a**. (A) 3D structure of the LiTryR:**9a** complex. LiTryR is shown as a yellow cartoon and its FAD cofactor and catalytic Cys residues are represented as orange sticks. **9a** is depicted as blue sticks. The 2F<sub>o</sub>-F<sub>c</sub> electron density map is shown as a purple mesh contoured at 0.9σ for **9a**. Relevant amino acids are displayed as capped sticks and labeled accordingly. (B) Superposition of **4a** and **9a** in complex with LiTryR. The LiTryR backbone is shown as a cartoon and colored white for clarity, its FAD cofactor is represented as light orange sticks. Ligands and relevant residues appear as sticks; **4a** is colored green and **9a** blue. The amino acids corresponding to a specific complex are colored according to the ligand present in the complex.

The displacements observed can be attributed to the different chemical groups in R<sub>2</sub>, and the presence/absence of an extra formal positive charge on the piperidine ring.



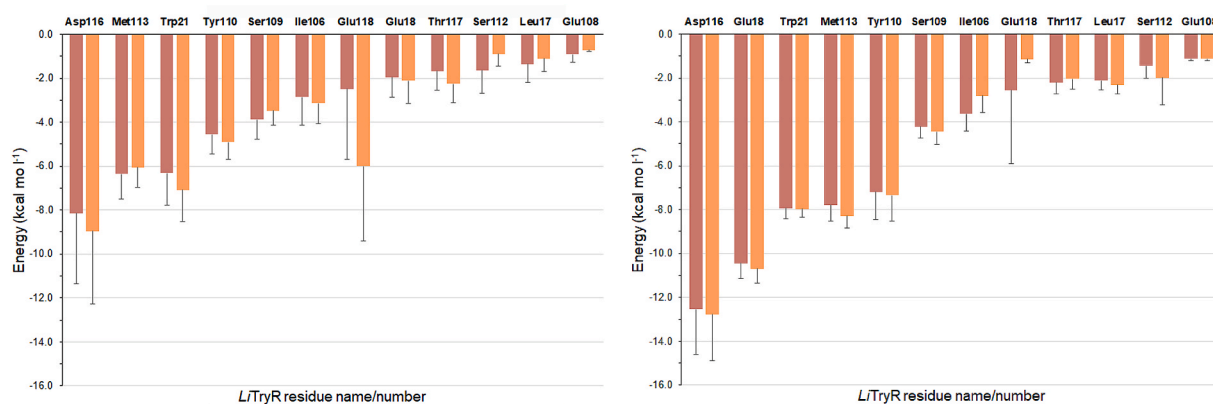
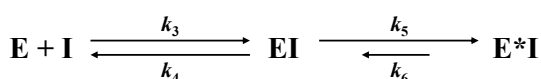


**Fig. 5.** Calculated average ( $\pm$ s.e.) contributions of individual *LiTryR* residues (monomers A and B in brown and orange, respectively) to the overall solvent-corrected interaction energies ( $\text{kcal mol}^{-1}$ ) with **4a** (top) and **9a** (bottom). For simplicity, a cutoff of 1.0 was used and bars were arranged in descending order of strength from left to right. The averages were calculated from a conformational ensemble made up of 20 snapshots taken every 5 ns from the post-equilibrated 10–110 ns interval of the MD trajectories and then cooled down to 273 K and energy minimized, as reported before [27].



**Scheme 3.** Two-step induced-fit mechanism of time-dependent inhibition of *LiTryR*. The initial step is a rapid equilibrium that leads to the formation of the enzyme-inhibitor (EI) encounter complex. The second phase involves a slow conformational transition of the enzyme to a higher affinity enzyme-inhibitor ( $\text{E}^*\text{I}$ ) complex. The formation and dissociation of EI and  $\text{E}^*\text{I}$  complexes are governed by association and dissociation rate constants  $k_3/k_4$  and  $k_5/k_6$ , respectively.

describes the distinctive curvature of the slow-binding inhibitors and allows the estimation –from the experimental data– of (i)  $v_i$  and  $v_s$ , and (ii) the apparent first-order rate constant for conversion from  $v_i$  to  $v_s$  ( $k_{\text{obs}}$ ) [44,45].

In the two-step induced-fit mechanism of time-dependent inhibition, the affinities of EI and  $\text{E}^*\text{I}$  complexes at a fixed substrate concentration are reflected by decreases in  $v_i$  and  $v_s$ , respectively, as a result of raising the inhibitor concentration [45]. The different  $v_i$  and  $v_s$  values obtained at fixed  $\text{TS}_2$  concentrations were subsequently used to estimate the apparent values of the inhibition constants for the initial EI complex ( $K_i^{\text{app}}$ ) and the high-affinity  $\text{E}^*\text{I}$  complex ( $K_i^{*\text{app}}$ ) (Equations (2) and (3)) (See Tables S3 and S4 in the Supplementary Material) [45].

The true  $K_i$  and  $K_i^*$  dissociation constants were obtained by fitting the  $K_i^{\text{app}}$  and  $K_i^{*\text{app}}$  values obtained at different  $\text{TS}_2$  concentrations to Equations (4) and (5), respectively. As shown in Fig. 6, both  $K_i^{\text{app}}$  and

$K_i^{*\text{app}}$  values increase as a curvilinear function of  $\text{TS}_2$ , thus demonstrating the mixed noncompetitive mode of *LiTryR* inhibition by the dimer disruptor **4c**. The estimated values obtained with these nonlinear regressions were  $1.2 \pm 0.1 \mu\text{M}$  for the  $K_i$  of the first equilibrium and  $0.2 \pm 0.01 \mu\text{M}$  for the overall  $K_i^*$  of the two-step induced-fit mechanism. As expected, the **4c**-induced isomerization of *LiTryR* leads to a much tighter binding complex. This is reflected in the submicromolar value obtained for the overall  $K_i^*$  of the two-step mechanism.

Because of the demonstrated capacity of **4c** to induce enzyme dissociation, the characteristic isomerization of the enzyme in this mechanism of slow-binding inhibition is expected to be related to homodimer disruption.

The comparable degree of curvature of the best-fit curves observed in both plots explains the high similarity between the estimated values of the thermodynamic cooperativity factors  $\alpha$  ( $5 \pm 1.3$ ) and  $\alpha^*$  ( $6.4 \pm 0.7$ ) characteristic of the fast and the global processes, respectively (Fig. 6).  $\alpha$  values higher than 1 but smaller than 10 indicate that the presence of substrate ( $\text{TS}_2$ ) in the active site impairs but clearly does not abolish binding of the inhibitor (**4c**). Interestingly, the  $\alpha$  values observed for the parent triazole-phenyl-thiazoles endowed with dimer disruption ability were approximately 1, which indicates that these inhibitors bind to the enzyme with similar affinity in the presence or in the absence of  $\text{TS}_2$ . This divergence suggests that the binding site of the triazolium salts and the triazole-phenyl-thiazoles in the encounter complex (EI) must be different.

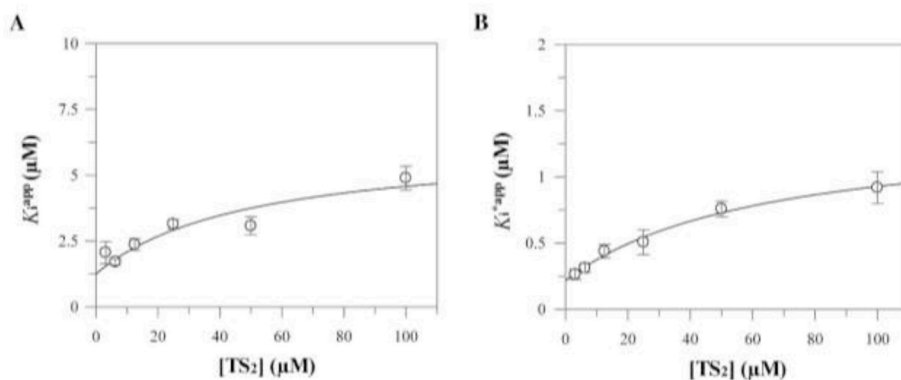


**Fig. 6.** Effect of substrate concentration on the apparent inhibition constants for the first equilibrium and the overall inhibitory process upon binding of **4c** to *LiTryR*. (A) Plot of the estimated values of  $K_i^{\text{app}}$  ( $\pm$  standard errors) as a function of  $\text{TS}_2$  concentration. The curve was fitted using Equation 4. (B) Plot of the estimated values of  $K_i^{*\text{app}}$  ( $\pm$  standard errors) as a function of  $\text{TS}_2$  concentration. The curve was fitted using Equation (5).

### 2.2.6. Binding mode of triazolium salts dimerization disruptors to LiTryR

All crystallization attempts with dimerization disruptors from series II were unsuccessful. Cocrystallization experiments –using inhibitor concentrations ranging from equimolar to 10-fold the molarity of LiTryR, for periods of 2–16 h at 4 °C– were not fruitful, whereas soaking experiments resulted in crystal cracking and blank diffraction patterns. The unfeasibility to obtain crystallographic structures of LiTryR in complex with the dimerization disruptors led us to use molecular modeling to elucidate the binding mode of these inhibitors. Taking into account the time-dependent inhibition mechanism of LiTryR inhibition by **4c** and given the structural similarity of compounds **4a** and **4c** (phenethyl and biphenethyl at R<sub>3</sub>, respectively), we simulated a model-built complex containing **4c** in a orientation similar to that observed for **4a** within the active site to address whether this might be the location of **4c** when the first EI complex is formed. As shown in Fig. 7, we observed an overall similar pattern but with the important addition that the range of interactions extended to the other enzyme subunit, most significantly those involving residues Phe396' and Leu399'. We took this as evidence that **4c** can then use the biphenyl substituent to get buried more deeply in a hydrophobic pocket and thereafter get access to the interfacial cavity described in our previous work as the putative binding location for the dimer disruptors of the triazole series [27].

To further assess this possibility, we built a model of LiTryR with **4c** bound inside the interfacial cavity, as done previously for the triazole derivatives [27], but bearing in mind that the methyl group on the triazolium ring should prevent formation of the proposed hydrogen bond between the triazole ring and the positive dipole of the short <sup>400</sup>MetGly<sup>405</sup> α-helix. Geometry optimization to allow mutual adaptation and the ensuing MD simulations supported the feasibility of this interfacial binding mode (Fig. 8A), which is dominated by many dispersion forces involving both subunits and strong electrostatic interactions with Asp432, Glu466 and Glu467 from one subunit as well as Asp432' from the other subunit (Fig. 8B).

Prompted by the strikingly different experimental results obtained in the dimerization assay (Table 1) for **4a** (inactive) and **4c** (active), despite their overall structural similarity (Scheme 1), we then decided to compute the free energy profile associated to shifting the ligand from the active site into the interfacial cavity using a reaction coordinate (RC). Our results (Fig. 9) clearly indicate that, whereas two local minima (designated M<sub>1</sub> and M<sub>2</sub>) are apparent for **4c** at the dimer interface, the energy surface for **4a** shows only metastable states (*i.e.*, no conspicuous local minima) and the energy increases sharply when the ligand approaches the cavity (*i.e.*, RC→0 Å). Therefore, **4a** would thermodynamically prefer to bind at the active site, as indeed found in our crystal structure, whereas gaining access into the cavity for **4c** and finding the

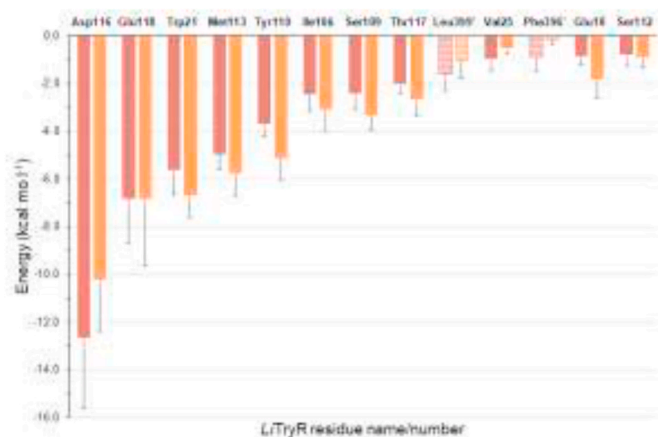


Fig. 7. Calculated average ( $\pm$ s.e.) contributions of individual LiTryR residues (monomers A and B in brown and orange, respectively) to the overall solvent-corrected interaction energies ( $\text{kcal mol}^{-1}$ ) with **4c**.

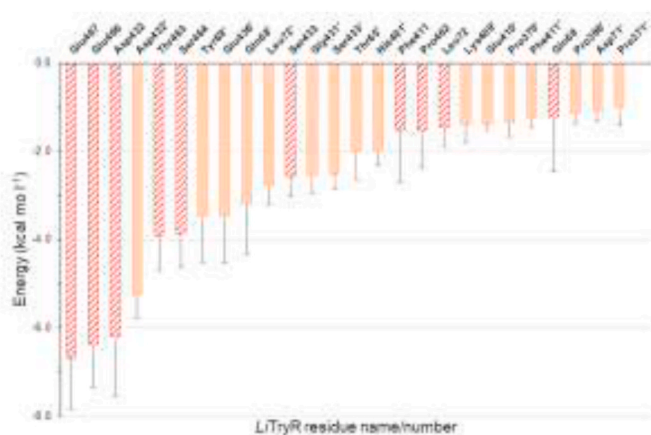
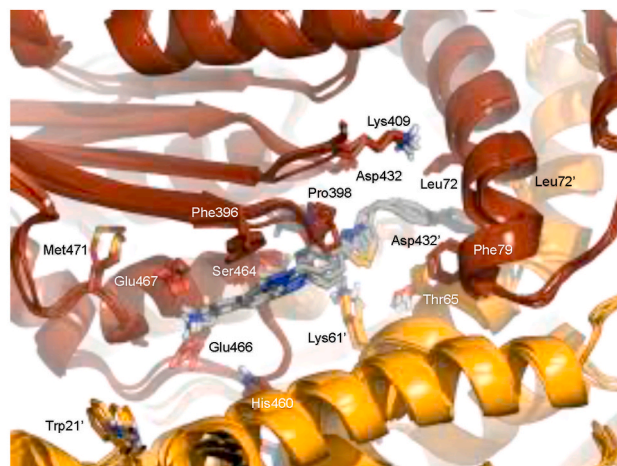
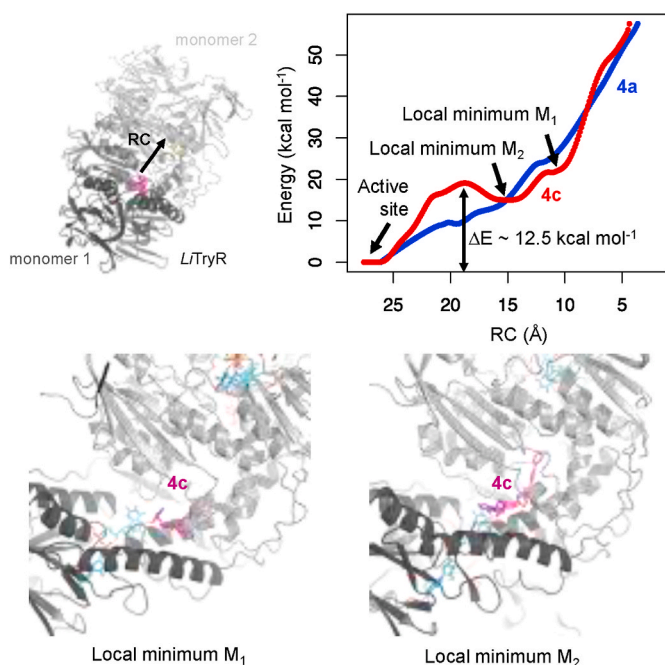


Fig. 8. (A) Cross-section of four overlaid energy-minimized snapshots from the simulated MD trajectory of the LiTryR:**4c** complex showing the ligand bound inside the interfacial cavity of the enzyme (ribbon representation, with monomers colored in brown and orange). Relevant protein residues have been labeled and the 399–407 stretch has been hidden from view to enhance clarity. (B) Calculated average ( $\pm$ s.e.) contributions of individual LiTryR residues (monomers A and B in different colors and patterns) to the overall solvent-corrected interaction energies ( $\text{kcal mol}^{-1}$ ) with **4c** when the ligand is bound at the subunit interface.

local minimum M<sub>1</sub> would require  $\sim 12.5 \text{ kcal mol}^{-1}$ . Visual inspection of the two energy minima (M<sub>1</sub> and M<sub>2</sub>) for **4c** confirms that in both cases the polar moieties of **4c** are projected into the solvent whereas the biphenyl substituent attached to the linker bonded to the thiazole ring is inserted as a protruding wedge into the interfacial cleft.

Thus, our hypothesis is that once **4c** reaches the M<sub>2</sub> state, the system would require some time for the integrity of the dimer to be affected, which is in consonance with the experimental kinetic evidence that demonstrates a time-dependent mode of enzyme inhibition.

Taken together, our computational data support our previous pharmacophore model for the parental triazole-phenyl-thiazole series [27] and confirm the crucial role of the elongated and bulky hydrophobic group attached to the end of the R<sub>3</sub> linker in the triazolium series for affecting LiTryR dimerization. We believe it is the balance between hydrophobic interactions at one end of the molecules and electrostatic interactions at the opposite end that determines the likelihood of deep penetration into the interfacial cavity, thus accounting for the lack of activity of **4a** and most of the other members of the series as disruptors of dimer integrity. In this respect, it is worth noticing the well-known interaction of biphenyl groups with lipid chains in a hydrophobic environment [51].



**Fig. 9.** Energy profile ( $\text{kcal mol}^{-1}$ ) theoretically calculated along the reaction coordinate used to bring **4a** (blue line) and **4c** (red line) from the active site ( $R > 25 \text{ \AA}$ ) into the cavity ( $R \rightarrow 0 \text{ \AA}$ ) at the *LiTryR* dimer interface by means of umbrella sampling MD simulations. A simplified molecular representation of the *LiTryR*:**4c** complex is shown for each local minimum.

### 2.2.7. Leishmanicidal activity and cytotoxicity

All the 1,2,3-triazolium salts were tested *in cellulo* to assess their potential as new leishmanicidal drug candidates. In the first phase of this screening campaign, the antileishmanial activity was monitored in axenic amastigotes of *L. infantum* by flow cytometry using the propidium iodide method whereas cytotoxicity was evaluated employing the human hepatoma cell line HepG2 by the crystal violet method. Treatments were performed at different concentrations ranging from 2.3 to 75  $\mu\text{M}$  over the course of 24 h. Half-maximal effective and cytotoxic concentrations ( $\text{EC}_{50}$  and  $\text{CC}_{50}$ , respectively) were compared to those of miltefosine and the representative parent triazoles **1a-e** [27] (Table 4).

According to these results, most of the novel 1,2,3-triazolium salts exhibit a leishmanicidal potency similar to that of their parent triazoles (**4b-e** vs **1b-e**), with the notable exception of **4a**, which showed a dramatic loss of activity compared to its parent triazole **1a**. On the other hand, compounds **4b-e** displayed significant lower cytotoxicity than their corresponding parent triazoles **1b-e**. These highly diminished cytotoxic activities result in a marked improvement of their selectivity indices (SIs).

Disubstituted thiazole analogues **4e,j-m** displayed high antileishmanial activities, with  $\text{EC}_{50}$  values against *L. infantum* axenic amastigotes in the 6–13  $\mu\text{M}$  range and SI values that oscillate between 4 and 12 (Table 4).

As previously observed in the parent triazole series [27], shortening the tetramethylene linker of the  $R_1$  substituent to a trimethylene improved the antileishmanial activity >2-fold despite the 4.5-fold loss of dimer disruption capacity (**4c** vs **4d**) (Table 4). Furthermore, compound **4d** showed the lowest  $\text{EC}_{50}$  value against *L. infantum* axenic amastigotes and the highest SI value among all the 1,2,3-triazolium salts.

1,2,3-triazolium salts **4b-e,j-l,n** showing  $\text{EC}_{50}$  values against *L. infantum* axenic amastigotes below 15  $\mu\text{M}$  and SI values above 5 were selected for the next step of the screening campaign. At this stage, the selected compounds were further tested for their leishmanicidal activity using THP-1 derived macrophages infected with *L. infantum* amastigotes expressing the green fluorescent protein (GFP). Infected cells were

**Table 4**

*In cellulo* activity on *L. infantum* axenic amastigotes and cytotoxicity of triazolium salt compounds II.

Compound	Series	$\text{EC}_{50}$ ( $\mu\text{M}$ ) <sup>b</sup>	$\text{CC}_{50}$ ( $\mu\text{M}$ ) <sup>c</sup>	SI <sup>d</sup>
Miltefosine <sup>a</sup>	–	$0.4 \pm 0.03$	>75	>187.5
Representative parent triazoles				
<b>1a</b> <sup>a</sup>	I	$13.9 \pm 0.6$	$20.3 \pm 2.4$	1.5
<b>1b</b> <sup>a</sup>	I	$15.3 \pm 1.7$	$33.3 \pm 2.7$	2.2
<b>1c</b> <sup>a</sup>	I	$11.6 \pm 0.8$	$43.1 \pm 2.6$	3.7
<b>1d</b> <sup>a</sup>	I	$5.2 \pm 0.3$	$60.4 \pm 3.4$	11.6
<b>1e</b> <sup>a</sup>	I	$15.6 \pm 3.0$	$26.5 \pm 4.1$	1.7
Triazolium salt analogues				
<b>4a</b>	II	$66.6 \pm 5.4$	>75	>1.1
<b>4b</b>	II	$12.9 \pm 0.5$	>75	>5.8
<b>4c</b>	II	$11.6 \pm 1.1$	>75	>6.5
<b>4d</b>	II	$4.8 \pm 0.3$	>75	>15.6
<b>4e</b>	II	$12.9 \pm 1.5$	>75	>5.8
Modifications at $R_1$ - $R_5$				
<b>3o</b>	II	>75	>75	<1.0
<b>4f</b>	II	$20.0 \pm 3.0$	>75	>3.8
<b>4g</b>	II	$7.6 \pm 0.3$	$35.9 \pm 3.5$	4.7
<b>4h</b>	II	$62.4 \pm 4.5$	>75	>1.2
<b>4i</b>	II	>75	>75	<1.0
<b>4j</b>	II	$6.4 \pm 0.4$	>75	>12.3
<b>4k</b>	II	$12.2 \pm 1.1$	>75	>6.1
<b>4l</b>	II	$6.0 \pm 0.4$	$46.5 \pm 7.4$	7.8
<b>4m</b>	II	$8.9 \pm 0.6$	$35.2 \pm 3.9$	4.0
<b>4n</b>	II	$14.0 \pm 1.1$	>75	>5.6
Modifications at $R_2$ (Scheme 2)				
<b>9a</b>	II	>75	>75	<1.0
<b>9b</b>	II	$28.4 \pm 2.8$	>75	>2.6

<sup>a</sup> Miltefosine and representative parent triazoles **1a-e** [27] were included as reference compounds.

<sup>b</sup> The half-maximal effective concentration ( $\text{EC}_{50}$ ) is defined as that causing a 50% reduction of proliferation in *L. infantum* amastigotes after a 24-h treatment. Results are representative of three independent experiments, each performed in triplicate.  $\text{EC}_{50} \pm \text{SE}$  values are indicated.

<sup>c</sup> The half-maximal cytotoxic concentration ( $\text{CC}_{50}$ ) is defined as that causing a 50% reduction of proliferation in human hepatocellular carcinoma (HepG2) cells after a 24-h treatment. Results are representative of three independent experiments.  $\text{CC}_{50} \pm \text{SE}$  values are indicated.

<sup>d</sup> Selectivity index (SI) is the ratio of  $\text{CC}_{50}$  against HepG2 cells relative to  $\text{EC}_{50}$  against *L. infantum* axenic amastigotes.

treated at different concentrations ranging from 2.3 to 75  $\mu\text{M}$  and monitored for 72 h. The relative number of amastigotes per cell at each condition was achieved using a slightly modified version of our previously reported protocol [27].  $\text{EC}_{50}$  and  $\text{CC}_{50}$  values are shown in Table 5 and compared to those of miltefosine and the representative parent triazoles **1a-e**.

The screened compounds could be divided into two groups: a first group including compounds **4b-d,n**, which were identified as dimer disruptors of *LiTryR*, and a second group including all the disubstituted thiazole analogues except **4m** (**4e,j-l**) that did not interfere with *LiTryR* dimerization.

According to the results shown in Table 5, the representative 1,2,3-triazolium salts **4b-d** showed highly enhanced leishmanicidal activities in intracellular amastigotes over those of their parent triazoles **1b-d**. Furthermore, the selectivity of these compounds was also dramatically improved due to their extremely low cytotoxicity, with  $\text{CC}_{50}$  values above 75  $\mu\text{M}$  (Table 5). This improvement in the antileishmanial activity and selectivity was more pronounced in compounds **4c,d** ( $\text{EC}_{50}$  values of 8.7 and 7.3  $\mu\text{M}$ , respectively) bearing a biphenylethyl group at the  $R_3$  substituent, with SI values above 8.6. Indeed, a similar selectivity improvement was also observed in the other dimer disruptor bearing a biphenylethyl at  $R_3$  (**4n**;  $\text{EC}_{50}$  value of 10  $\mu\text{M}$ ; SI = 6.4) (Table 5).

All in all, a strong correlation between the dimer disruption ability of 1,2,3-triazolium salts and their antileishmanial activity against intracellular amastigotes was observed. Accordingly, the most potent dimer disruptors (**4c**, and to a lesser extent **4d** and **4n**, all of them bearing a

**Table 5**Activity on *L. infantum* intracellular amastigotes and cytotoxic activity of triazolium salt compounds II.

Compound	Series	EC <sub>50</sub> (μM) <sup>b</sup>	CC <sub>50</sub> (μM) <sup>c</sup>	SI <sup>d</sup>
Miltefosine <sup>a</sup>	–	0.6 ± 0.1	>75	>125
Representative parent triazoles				
1a <sup>a</sup>	I	29.4 ± 3.1	27.8 ± 3.6	<1.0
1b <sup>a</sup>	I	>75	29.0 ± 4.7	<1.0
1c <sup>a</sup>	I	52.1 ± 5.1	40.5 ± 0.8	<1.0
1d <sup>a</sup>	I	>75	37.3 ± 5.2	<1.0
1e <sup>a</sup>	I	24.2 ± 5.6	>75	>3.1
Triazolium salt analogues				
4b	II	27.0 ± 5.5	>75	>2.8
4c	II	8.7 ± 0.6	>75	>8.6
4d	II	7.3 ± 1.0	>75	>10.3
4e	II	73.8 ± 3.9	>75	<1.0
Modifications at R <sub>1</sub> -R <sub>5</sub>				
4j	II	14.1 ± 3.0	34.5 ± 1.7	2.4
4k	II	15.0 ± 2.8	42.6 ± 3.8	2.8
4l	II	24.2 ± 0.8	54.5 ± 2.3	2.2
4n	II	10.0 ± 1.2	63.8 ± 6.0	6.4

<sup>a</sup> Miltefosine and representative parent triazoles **1a–e** were included as reference compounds.

<sup>b</sup> The EC<sub>50</sub> is defined as that causing a 50% reduction in the number of *L. infantum* amastigotes per THP-1-derived macrophage in the culture after a 72-h treatment. Living intracellular amastigotes were identified by their green fluorescence due to GFP expression and their lack of permeability to propidium iodide. Results are representative of three independent experiments. EC<sub>50</sub> ± SE values are indicated.

<sup>c</sup> CC<sub>50</sub> is defined as that causing a 50% reduction of proliferation in HepG2 cells after a 72-h treatment. Results are representative of three independent experiments. CC<sub>50</sub> ± SE values are indicated.

<sup>d</sup> SI is the ratio of CC<sub>50</sub> against HepG2 cells relative to EC<sub>50</sub> against *L. infantum* intracellular amastigotes.

biphenylethyl at R<sub>3</sub>) showed the best EC<sub>50</sub> values and can be considered the most promising candidates for the development of a leishmanicidal drug.

To gain additional evidence on the capacity of the intrinsically fluorescent **4c** to cross cell membranes, its intracellular localization in the parasites was demonstrated by fluorescence microscopy (see Fig. S12 in the Supplementary Material).

### 2.2.8. Measurement of non-protein thiols in *L. infantum* promastigotes

Demonstration of “on-target” mechanisms of action is critical to determine the suitability of small molecules as preclinical candidates in target-based drug discovery [52]. In the case of TryR, this demonstration is challenging due to (i) the high T(SH)<sub>2</sub> concentrations found in *Leishmania* parasites [53,54], and (ii) the high level of TryR inhibition that is required for effectively affecting the growth rate of trypanosomatids [14,55]. Therefore, attributing any biological effect on whole parasites to TryR inhibition or to any T(SH)<sub>2</sub>-dependent downstream effector has to be taken with caution.

Despite these drawbacks and because TryR is the main regulator of leishmanial thiol metabolism, assessment of LiTryR as the main molecular target of the optimized 1,2,3-triazolium salt **4c** was evaluated by analyzing the non-protein thiol content of *L. infantum* promastigotes by flow cytometry using 5-chloromethylfluorescein (CMF) diacetate as the probe. A ~20% reduction in the CMF-derived fluorescence was observed upon treatment of *L. infantum* promastigotes with 75 μM of **4c** for 1 h (Fig. 10). Although this might seem a non-relevant reduction in the total thiol content in the cells, it must be borne in mind that a high degree of T(SH)<sub>2</sub> oxidation is not expected in parasites grown for 1 h in the absence of any source of oxidative stress. Accordingly, even a high degree of TryR inhibition during this period is not expected to lead to a strong reduction in the intracellular thiol levels.

To stimulate T(SH)<sub>2</sub> consumption, we repeated the experiment in the presence of moderate concentrations (625 μM) of hydrogen peroxide (H<sub>2</sub>O<sub>2</sub>). Surprisingly, H<sub>2</sub>O<sub>2</sub> treatment did not decrease the total thiol

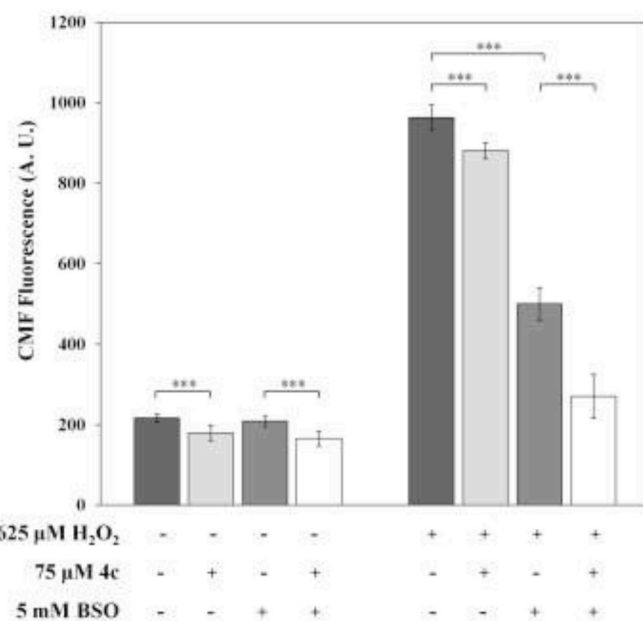


**Fig. 10.** Effect of the triazolium salt **4c** on the non-protein thiol content of *L. infantum* promastigotes. Parasites were treated with the vehicle of the treatments (black bars), 75 μM of **4c** for 1 h (light grey bars), 5 mM of BSO for 72 h (dark grey bars) and the combined treatment (white bars). Non-protein thiols of *L. infantum* promastigotes were estimated by flow cytometry using the CMF diacetate dye, whose green fluorescence was detected and quantified in living parasites excluding the propidium iodide dye. Mean values of nine independent experiments are displayed in bar graphs. Error bars represent the 99.0% confidence intervals calculated for each mean. \*\*\* p-value < 0.001.

content in the parasites. On the contrary, our results demonstrate a ~5-fold increase (from ~200 to ~1000 A U.) in the CMF-derived fluorescence, which is indicative of a strong stimulation of *de novo* thiol synthesis. Additional treatment with **4c** caused ~15% reduction in the CMF-derived fluorescence.

In order to characterize the observed H<sub>2</sub>O<sub>2</sub>-induced *de novo* thiol synthesis, we performed the same experiments on parasites previously exposed to D,L-buthionine-(S,R)-sulfoximine (BSO) [56]. BSO is a well-known inhibitor of γ-glutamylcysteine synthetase, the rate-limiting enzyme of GSH synthesis [57], although it has also been described as an inhibitor of *T. cruzi* trypanothione synthetase [58]. Incubation of *L. infantum* promastigotes with BSO was performed at a concentration of 5 mM for 72 h, a period of time in which parasite growth is not affected. As shown in Fig. 10, BSO treatment reduced to 50% (~500 A U.) the CMF-derived fluorescence in the H<sub>2</sub>O<sub>2</sub>-treated parasites. This result strongly supports the notion that moderate oxidative stress conditions induce synthesis of GSH, and presumably T(SH)<sub>2</sub>, in *L. infantum* parasites. Very significantly, exposure of the BSO-treated parasites to **4c** under the H<sub>2</sub>O<sub>2</sub>-induced oxidative conditions caused an additional 50% reduction (~250 A U.) in the fluorescence signal, which supports a strong inhibitory effect of this compound on the LiTryR activity inside the parasites. Additionally, these results attest to the essential role of T(SH)<sub>2</sub> *de novo* synthesis and regeneration in increasing the non-protein thiol content of *L. infantum* promastigotes as an adaptation to oxidative stress, therefore supporting the evaluation of concomitant treatments aimed at simultaneously blocking both processes in the parasites.

### 3. Conclusions

N-alkylation of most of our previously described triazole-based LiTryR inhibitors strongly modifies their behavior and turns their inhibition modality from noncompetitive to competitive. Both the enzymatic and crystallographic studies reported so far support this change.

On the other hand, only three derivatives bearing a biphenylethyl substituent at R<sub>3</sub> maintain the characteristic strong LiTryR dimerization disruption ability of their parent triazoles. In general, the new triazolium salts maintain the potency of their precursors against axenic amastigotes but their toxicity against the human cell line HepG2 is highly reduced and, most importantly, their activity against intracellular amastigotes is strongly reinforced. Significantly, the three derivatives able to disrupt the homodimeric nature of the enzyme show EC<sub>50</sub> values below 10 μM in the cell infection assay and are endowed with extremely low host cell toxicities (CC<sub>50</sub> values above 75 μM). The optimized 1,2,3-triazolium salt **4c** is able to reduce by 50% the non-protein thiol content of *L. infantum* promastigotes grown under mild oxidative stress conditions in the presence of BSO. This novel finding provides strong evidence of its capacity to inhibit LiTryR inside the parasites. To the best of our knowledge, **4c** is one of the very few TryR inhibitors for which a relevant effect on the intracellular thiol content has been demonstrated. All in all, our results suggest that triazolium salt derivatives **4c** and **4d** may be promising compounds for further drug development.

## 4. Experimental

### 4.1. Chemistry

Experiments dealing with air- and/or water-sensitive reagents/compounds were performed under argon atmosphere. Hygroscopic species were previously dried under vacuum for 24 h by using P<sub>2</sub>O<sub>5</sub> as the drying agent. Unless otherwise noted, analytical grade solvents and commercially available reagents were used without further purification. Anhydrous CH<sub>2</sub>Cl<sub>2</sub> was dried by refluxing over CaH<sub>2</sub>. Anhydrous DMF was commercially available. THF was dried by reflux over Na and benzophenone. Lyophilizations were carried out on a *Telstar 6–80* lyophilizer.

Monitoring of the reactions was performed by: a) analytical thin-layer chromatography (TLC) on silica gel 60 F<sub>254</sub> (Merck, Darmstadt, Germany); b) High Performance Liquid Chromatography coupled to Mass Spectrometry (HPLC-MS) using a Waters Alliance 2695 Separation Module with Waters Micromass ZQ Detector; or c) Analytical HPLC in a Waters 600 equipped with a C18 Sunfire column (4.6 mm × 150 mm, 3.5 μm) and a selectable wavelength UV detector.

Compounds were purified by: a) flash column chromatography (Merck, Darmstadt, Germany) with Silica gel 60 (230–400 mesh); b) Centrifugal Circular Thin-Layer Chromatography (CCTLC) on a Chromatotron™ (Kiesegel 60 PF<sub>254</sub> gipshaltig (Merck, Darmstadt, Germany)), with layer thicknesses of 1 and 2 mm and flow rates of 2 and 3 mL/min, respectively, or c) High Performance Flash column chromatography (HPFC) on a Biotage *Isolera One* using KP-C18-HS flash cartridges of 12g (21 × 55 mm) for the reverse phase.

The purity of the compounds was checked by analytical HPLC on a Waters 600 system equipped with a C18 Sunfire column (4.6 mm × 150 mm, 3.5 μm) and a selectable wavelength UV detector. Alternatively, an Agilent Technologies 1120 Compact LC provided by a reverse-phase column *ACE 5 C18-300* (4.6 mm × 150 mm, 3.5 μm) and integrated diode detector *PDA 996* was used. As mobile phase mixtures of A: CH<sub>3</sub>CN and B: H<sub>2</sub>O (0.05% of TFA) on gradient mode with a flow rate of 1 mL/min were used. Gradient A from 10% of A to 100% of A in 10 min was used. The purity of the final compounds was also determined to be >95% by elemental analysis with a LECO *CHNS-932* apparatus. Deviations of the elemental analysis results from the calculated value were within ±0.4%.

Melting points (M.p) were measured on a *Mettler Toledo M170* apparatus and are uncorrected. Mass Spectrum (MS) on Electrospray (ESI) mode was registered in a *Hewlett-Packard 1100SD* in positive mode. High-resolution mass spectra (HMRS) were obtained in an *Agilent 6520 Accurate-Mass Q-TOF LC-MS* equipped with a liquid chromatograph *HP-1200* (Agilent Technologies, Santa Clara, CA) coupled to a mass spectrometer with hybrid mass analyzer *Q-TOF 6520*. Usually, an error equal

or lower than 5 ppm was allowed. Nuclear Magnetic Resonance (NMR) spectra were recorded on a Varian INNOVA-300 operating at 300 MHz (<sup>1</sup>H) and 75 MHz (<sup>13</sup>C), Varian INNOVA-400 operating at 400 MHz (<sup>1</sup>H) and 100 MHz (<sup>13</sup>C), Varian MERCURY-400 operating at 400 MHz (<sup>1</sup>H) and 100 MHz (<sup>13</sup>C) and a Varian SYSTEM-500 operating at 500 MHz (<sup>1</sup>H) and 125 MHz (<sup>13</sup>C). The assignments were performed by means of different standard homonuclear and heteronuclear correlation experiments (gHSQC, gHMBC and NOESY) when required.

#### 4.1.1. General procedure for the N-alkylation of 1,2,3-triazole-phenyl-thiazole compounds

To a solution of the corresponding N-Cbz protected intermediate triazoles (1 eq) in dry CH<sub>2</sub>Cl<sub>2</sub>, methyl trifluoromethanesulfonate or ethyl trifluoromethanesulfonate (1 eq) were added and the reaction mixture was stirred at room temperature for 15 min under an argon atmosphere. Then, the reaction was quenched with MeOH (10 mL) and H<sub>2</sub>O (5 mL), and evaporated to dryness. The final residue was purified by CCTLC on the Chromatotron (eluent are specified in each case) and the compounds were isolated as trifluoromethanesulfonate (TfO) salts.

#### 4.1.2. 4-(4-(((Benzyloxy)carbonyl)amino)butyl)-3-methyl-1-(3-(2-(2-oxoimidazolidin-1-yl)ethoxy)-4-(4-phenethylthiazol-2-yl)phenyl)-1H-1,2,3-triazol-3-ium trifluoromethanesulfonate (**3a**)

Following the general procedure of N-alkylation, a solution of triazole **2a** [27] (150 mg, 0.23 mmol) in anhydrous CH<sub>2</sub>Cl<sub>2</sub> (15 mL) was treated with methyl trifluoromethanesulfonate (25 μL, 0.23 mmol). After the work-up, the final residue was purified by CCTLC on the Chromatotron (CH<sub>2</sub>Cl<sub>2</sub>/MeOH, 95:5) to provide 159 mg (85%) of **3a** as a yellow oil. Spectroscopic data are included in the Supplementary Material. HRMS (ES, positive mode) *m/z*: calculated for C<sub>37</sub>H<sub>42</sub>N<sub>7</sub>O<sub>4</sub>S 680.3019; found 680.3019 (0.01 ppm).

#### 4.1.3. 4-(4-(((Benzyloxy)carbonyl)amino)butyl)-3-methyl-1-(4-(4-(2-naphthalen-2-yl)vinyl)thiazol-2-yl)-3-(2-(2-oxoimidazolidin-1-yl)ethoxy)phenyl)-1H-1,2,3-triazol-3-ium trifluoromethanesulfonate (**3b**)

A solution of triazole **2b** [27] (67 mg, 0.09 mmol) in anhydrous CH<sub>2</sub>Cl<sub>2</sub> (5 mL) was reacted with methyl trifluoromethanesulfonate (11 μL, 0.09 mmol) following the general N-alkylation procedure. After the work-up, the final residue was purified by CCTLC on the Chromatotron (CH<sub>2</sub>Cl<sub>2</sub>/MeOH, 95:5) affording 68 mg (82%) of a yellow oil identified as **3b**. Spectroscopic data are included in the Supplementary Material. HRMS (ES, positive mode) *m/z*: calculated for C<sub>41</sub>H<sub>42</sub>N<sub>7</sub>O<sub>4</sub>S 728.3019; found 728.3022 (0.39 ppm).

#### 4.1.4. 1-(4-(4-(2-([1,1'-Biphenyl]-4-yl)vinyl)thiazol-2-yl)-3-(2-(2-oxoimidazolidin-1-yl)ethoxy)phenyl)-4-(4-(((benzyloxy)carbonyl)amino)butyl)-3-methyl-1H-1,2,3-triazol-3-ium trifluoromethanesulfonate (**3c**)

Following the general N-alkylation procedure, a solution of triazole **2c** [27] (90 mg, 0.12 mmol) in anhydrous CH<sub>2</sub>Cl<sub>2</sub> (12 mL) was reacted with methyl trifluoromethanesulfonate (14 μL, 0.12 mmol). After the work-up, the final residue was purified by CCTLC on the Chromatotron (CH<sub>2</sub>Cl<sub>2</sub>/MeOH, 94:6) to provide 77 mg (70%) of **3c** as a yellow oil. Spectroscopic data are included in the Supplementary Material. HRMS (ES, positive mode) *m/z*: calculated for C<sub>43</sub>H<sub>44</sub>N<sub>7</sub>O<sub>4</sub>S 754.3176; found 754.3197 (2.81 ppm).

#### 4.1.5. (E)-1-(4-(4-(2-([1,1'-Biphenyl]-4-yl)vinyl)thiazol-2-yl)-3-(2-(2-oxoimidazolidin-1-yl)ethoxy)phenyl)-4-(3-(((benzyloxy)carbonyl)amino)propyl)-3-methyl-1H-1,2,3-triazol-3-ium trifluoromethanesulfonate (**3d**)

Following the general procedure of triazole N-alkylation, a solution of triazole **2d** [27] (111 mg, 0.15 mmol) in anhydrous CH<sub>2</sub>Cl<sub>2</sub> (15 mL) was reacted with methyl trifluoromethanesulfonate (17 μL, 0.15 mmol). The final residue was purified by CCTLC on the Chromatotron (CH<sub>2</sub>Cl<sub>2</sub>/MeOH, 95:5) to provide 115 mg (85%) of a yellow oil identified as **3d**. Spectroscopic data are included in the Supplementary Material. HRMS (ES, positive mode) *m/z*: calculated for C<sub>42</sub>H<sub>42</sub>N<sub>7</sub>O<sub>4</sub>S 740.3019;

found 740.3023 (0.51 ppm).

**4.1.6. 4-(4-(((Benzyloxy)carbonyl)amino)butyl)-1-(4-(4,5-diphenylthiazol-2-yl)-3-(2-(2-oxoimidazolidin-1-yl)ethoxy)phenyl)-3-methyl-1H-1,2,3-triazol-3-ium trifluoromethanesulfonate (3e)**

Following the general procedure of *N*-alkylation, a solution of triazole **2e** [27] (90 mg, 0.13 mmol) in anhydrous CH<sub>2</sub>Cl<sub>2</sub> (11 mL) was treated with methyl trifluoromethanesulfonate (14 μL, 0.13 mmol). After the work-up, the final residue was purified by CCTLC on the Chromatotron (CH<sub>2</sub>Cl<sub>2</sub>/MeOH, 93:7) to afford 96 mg (87%) of a yellow oil identified as **3e**. Spectroscopic data are included in the Supplementary Material. HRMS (ES, positive mode) *m/z*: calculated for C<sub>41</sub>H<sub>42</sub>N<sub>7</sub>O<sub>4</sub>S 728.3019; found 728.3048 (3.91 ppm).

**4.1.7. General procedure for *N*-Cbz deprotection and hydrogenation reactions**

A solution of the corresponding protected triazolium salts compounds **3a-e** (1 eq) in a 1:1 mixture of THF/MeOH (20 mL) containing Pd/C (10%) (20% wt/wt) and TFA (0.5–1.5 mL) was hydrogenated at room temperature overnight under atmospheric pressure using a balloon filled with hydrogen gas (3 cycles of vacuum + hydrogen). The Pd/C was filtered through Whatman PTFE filter paper, the solvent was removed under reduced pressure and was co-evaporated with mixtures of CH<sub>2</sub>Cl<sub>2</sub>/MeOH (5 × 10 mL). The residue was purified by HPFC on a SP1 Isolera Biotage using reverse phase columns (H<sub>2</sub>O/acetonitrile from 100:0 to 0:100 in 45 min) to afford the final deprotected compounds as TFA and TfO double salts. In compounds **3b-d** the double bond at the thiazole substituent was simultaneously hydrogenated in these reaction conditions.

**4.1.8. 4-(4-Ammoniobutyl)-3-methyl-1-(3-(2-(2-oxoimidazolidin-1-yl)ethoxy)-4-(4-phenethylthiazol-2-yl)phenyl)-1H-1,2,3-triazol-3-ium 2,2,2-trifluoroacetate trifluoromethanesulfonate (4a)**

Following the general deprotection procedure a solution of **3a** (88 mg, 0.11 mmol), Pd/C 10% (18 mg) and TFA (0.7 mL) in a 1:1 mixture of THF/MeOH (20 mL) was hydrogenated. The final residue was purified by reverse phase on a Biotage to yield 31 mg (36%) of a yellow oil identified as **4a**. Spectroscopic data are included in the Supplementary Material. HPLC (*Gradient A, Agilent*): *R<sub>t</sub>* = 6.7 min; HRMS (ES, positive mode) *m/z*: calculated for C<sub>29</sub>H<sub>36</sub>N<sub>7</sub>O<sub>2</sub>S 546.2651; found 546.2660 (1.59 ppm); Anal. Calc. for C<sub>29</sub>H<sub>36</sub>N<sub>7</sub>O<sub>2</sub>S.TFA.TfO: C. 47.46; H. 4.61; N. 12.11; S. 7.92; found: C. 47.84; H. 4.73; N. 12.05; S. 7.53.

**4.1.9. 4-(4-Ammoniobutyl)-3-methyl-1-(4-(2-(naphthalen-2-yl)ethyl)thiazol-2-yl)-3-(2-(2-oxoimidazolidin-1-yl)ethoxy)phenyl)-1H-1,2,3-triazol-3-ium 2,2,2-trifluoroacetate trifluoromethanesulfonate (4b)**

Following the general deprotection procedure, a solution of **3b** (160 mg, 0.18 mmol), Pd/C 10% (32 mg) and TFA (1.0 mL) in a 1:1 mixture of THF/MeOH (30 mL) was hydrogenated. The final residue was purified by Biotage to provide 78 mg (50%) of **4b** a yellow oil. Spectroscopic data are included in the Supplementary Material. HPLC (*Gradient A, Agilent*): *R<sub>t</sub>* = 7.1 min; HRMS (ES, positive mode) *m/z*: calculated for C<sub>33</sub>H<sub>38</sub>N<sub>7</sub>O<sub>2</sub>S 596.2808; found 596.2787 (−3.4 ppm); Anal. Calc. for C<sub>33</sub>H<sub>38</sub>N<sub>7</sub>O<sub>2</sub>S.TFA.TfO: C. 50.29; H. 4.57; N. 11.40; S. 7.46; found: C. 50.05; H. 5.08; N. 10.92; S. 7.83.

**4.1.10. 1-(4-(4-(2-([1,1'-Biphenyl]-4-yl)ethyl)thiazol-2-yl)-3-(2-(2-oxoimidazolidin-1-yl)ethoxy)phenyl)-4-(4-ammoniobutyl)-3-methyl-1H-1,2,3-triazol-3-ium 2,2,2-trifluoroacetate trifluoromethanesulfonate (4c)**

Following the general deprotection procedure, a solution of **3c** (148 mg, 0.2 mmol), Pd/C 10% (30 mg) and TFA (1 mL) in a 1:1 mixture of THF/MeOH (30 mL) was hydrogenated. The final residue was purified by reverse phase on a Biotage to give 53 mg (31%) of **4c** as a yellow oil. Spectroscopic data are included in the Supplementary Material. HPLC (*Gradient A, Agilent*): *R<sub>t</sub>* = 7.7 min; HRMS (ES, positive mode) *m/z*: calculated for C<sub>35</sub>H<sub>40</sub>N<sub>7</sub>O<sub>2</sub>S 622.2964; found 622.2952 (−2.02 ppm);

Anal. Calc. for C<sub>35</sub>H<sub>40</sub>N<sub>7</sub>O<sub>2</sub>S.TFA.TfO: C. 51.52; H. 4.67; N. 11.07; S. 7.24; found: C. 51.88; H. 5.25; N. 10.78; S. 7.61.

**4.1.11. 1-(4-(4-(2-([1,1'-Biphenyl]-4-yl)ethyl)thiazol-2-yl)-3-(2-(2-oxoimidazolidin-1-yl)ethoxy)phenyl)-4-(3-ammoniopropyl)-3-methyl-1H-1,2,3-triazol-3-ium 2,2,2-trifluoroacetate trifluoromethanesulfonate (4d)**

Following the general deprotection procedure, a solution of **3d** (115 mg, 0.13 mmol), Pd/C 10% (23 mg) and TFA (0.8 mL) in a 1:1 mixture of THF/MeOH (25 mL) was hydrogenated. After the work-up, the final residue was purified by reverse phase on a Biotage to provide 10 mg (10%) of **4d** as a yellow oil identified. Spectroscopic data are included in the Supplementary Material. HPLC (*Gradient A, Agilent*): *R<sub>t</sub>* = 7.6 min; HRMS (ES, positive mode) *m/z*: calculated for C<sub>34</sub>H<sub>38</sub>N<sub>7</sub>O<sub>2</sub>S 608.2808; found 608.2814 (0.99 ppm); Anal. Calc. for C<sub>34</sub>H<sub>38</sub>N<sub>7</sub>O<sub>2</sub>S.TFA.TfO: C. 50.97; H. 4.51; N. 11.25; S. 7.35; found: C. 50.32; H. 4.83; N. 11.38; S. 7.34.

**4.1.12. 4-(4-Ammoniobutyl)-1-(4-(4,5-diphenylthiazol-2-yl)-3-(2-(2-oxoimidazolidin-1-yl)ethoxy)phenyl)-3-methyl-1H-1,2,3-triazol-3-ium 2,2,2-trifluoroacetate trifluoromethanesulfonate (4e)**

According to the general deprotection procedure, a solution of **3e** (96 mg, 0.11 mmol), Pd/C 10% (19 mg) and TFA (0.9 mL) in a 1:1 mixture of THF/MeOH (25 mL) was hydrogenated. The final residue was purified by Biotage providing 15 mg (16%) of a yellow oil identified as **4e**. Spectroscopic data are included in the Supplementary Material. HPLC (*Gradient A, Agilent*): *R<sub>t</sub>* = 7.2 min; HRMS (ES, positive mode) *m/z*: calculated for C<sub>33</sub>H<sub>36</sub>N<sub>7</sub>O<sub>2</sub>S 594.2651; found 594.2649 (−0.43 ppm); Anal. Calc. for C<sub>33</sub>H<sub>36</sub>N<sub>7</sub>O<sub>2</sub>S.TFA.TfO: C. 50.40; H. 4.35; N. 11.43; S. 7.47; found: C. 49.86; H. 4.31; N. 11.63; S. 7.36.

**4.1.13. Benzyl 4-(1-(3-hydroxy-4-(4-phenethylthiazol-2-yl)phenyl)-1H-1,2,3-triazol-4-yl)butyl) carbamate (5)**

In a 100 mL conical flask, under an argon atmosphere, methoxylated compound **2f** [27] (400 mg, 0.7 mmol, 1 eq) was dissolved in dry CH<sub>2</sub>Cl<sub>2</sub> (20 mL) and cooled at −78 °C using an acetone/dry ice bath. Then, a 1 M solution of BBr<sub>3</sub> in CH<sub>2</sub>Cl<sub>2</sub> (12 mL, 7 mmol, 10 eq) was added dropwise. After 45 min, a second dropwise addition of 1 M solution of BBr<sub>3</sub> in CH<sub>2</sub>Cl<sub>2</sub> (12 mL, 7 mmol, 10 eq) was done. The reaction mixture was stirred at −78 °C for 4 h, and then, was quenched with MeOH and water for 5 min under cooling. The reaction was stirred at room temperature overnight to completely remove the boron complexes formed. Finally, the reaction mixture was concentrated under reduced pressure and the residue was extracted with CH<sub>2</sub>Cl<sub>2</sub> (3 × 20 mL), dried over Na<sub>2</sub>SO<sub>4</sub>, filtered and evaporated to dryness. The final residue was purified by flash column chromatography in silica gel (from CH<sub>2</sub>Cl<sub>2</sub>/MeOH 100:0.4 to 100:1.5) to give 240 mg (62%) of the phenol derivative **5** as a yellow oil. Spectroscopic data are included in the Supplementary Material. HRMS (ES, positive mode) *m/z*: calculated for C<sub>31</sub>H<sub>32</sub>N<sub>5</sub>O<sub>3</sub>S 554.2220; found 554.2226 (1.03 ppm).

**4.1.14. Benzyl 4-(2-((methylsulfonyl)oxy)ethyl)piperidine-1-carboxylate (6a)**

To a solution of the commercially available benzyl 4-(2-hydroxyethyl)piperidine-1-carboxylate (230 mg, 0.87 mmol) in dry CH<sub>2</sub>Cl<sub>2</sub> (5 mL) under an argon atmosphere at 0 °C, a solution of methanesulfonylchloride (67 μL, 0.87 mmol), dry NEt<sub>3</sub> (121 μL, 0.87 mmol) and DMAP (11 mg, 0.087 mmol) in dry CH<sub>2</sub>Cl<sub>2</sub> (2 mL) were added. The reaction mixture was stirred at room temperature overnight, and then, the reaction was diluted with water. After extraction with CH<sub>2</sub>Cl<sub>2</sub> (3 × 10 mL), the organic layer was dried (Na<sub>2</sub>SO<sub>4</sub>), filtered and evaporated to dryness to give 215 mg (72%) of the mesyl intermediate **6a** as a colourless oil. This intermediate was used without prior purification in the next reaction step. Spectroscopic data are included in the Supplementary Material. These data are in agreement with literature data [42].

#### 4.1.15. Benzyl 4-(((methylsulfonyl)oxy)methyl)piperidine-1-carboxylate (**6b**)

Following a similar procedure to that described for intermediate **6a**, commercially available benzyl 4-(hydroxymethyl)piperidine-1-carboxylate (217 mg, 0.87 mmol) in dry CH<sub>2</sub>Cl<sub>2</sub> (5 mL) was treated with a solution of methanesulfonylchloride (67  $\mu$ L, 0.87 mmol), dry NEt<sub>3</sub> (121  $\mu$ L, 0.87 mmol) and DMAP (11 mg, 0.087 mmol) in dry CH<sub>2</sub>Cl<sub>2</sub> (2 mL) at room temperature overnight. After the work-up, 243 mg (85%) of the mesyl intermediate **6b** was obtained as a colourless oil. This intermediate was used without prior purification in the next reaction step. Spectroscopic data are included in the Supplementary Material. These data are in agreement with literature data [43].

#### 4.1.16. Benzyl 4-(2-(5-(4-(4-(((benzyloxy)carbonyl)amino)butyl)-1H-1,2,3-triazol-1-yl)-2-(4-phenethylthiazol-2-yl)phenoxy)ethyl)piperidine-1-carboxylate (**7a**)

To a solution of the phenol intermediate **5** (50 mg, 0.09 mmol) and K<sub>2</sub>CO<sub>3</sub> (30.4 mg, 0.11 mmol) in dry DMF (3 mL) at 50 °C, the mesyl derivative **6a** (33.8 mg, 0.099 mmol) dissolved in dry DMF (1 mL) was added. The reaction mixture was stirred at 80 °C for 3 h. The mixture was cooled to room temperature, and the solvent was removed in vacuum. The crude was redissolved in CH<sub>2</sub>Cl<sub>2</sub> (20 mL) and washed with water (2  $\times$  20 mL). The organic layer was dried (Na<sub>2</sub>SO<sub>4</sub>), filtered and evaporated to dryness. The final residue was purified by flash column chromatography on silica gel (Hexane/ethyl acetate, 3:1 to 1:2) to give 42 mg (58%) of **7a** as a colourless oil. Spectroscopic data are included in the Supplementary Material. HRMS (ES, positive mode) *m/z*: calculated for C<sub>46</sub>H<sub>50</sub>N<sub>6</sub>O<sub>5</sub>S 798.3563; found 798.3571 (0.90 ppm).

#### 4.1.17. Benzyl 4-((5-(4-(4-(((benzyloxy)carbonyl)amino)butyl)-1H-1,2,3-triazol-1-yl)-2-(4-phenethylthiazol-2-yl)phenoxy)methyl)piperidine-1-carboxylate (**7b**)

To a solution of the phenol intermediate **5** (100 mg, 0.18 mmol) and K<sub>2</sub>CO<sub>3</sub> (30.4 mg, 0.22 mmol) in dry DMF (5 mL) at 50 °C, a solution of the mesyl derivative **6b** (64.8 mg, 0.198 mmol) in dry DMF (2 mL) was added. The reaction mixture was stirred at 80 °C for 3 h. The mixture was cooled to room temperature, and the solvent was concentrated to dryness. The residue was redissolved in CH<sub>2</sub>Cl<sub>2</sub> (20 mL) and washed with water (2  $\times$  20 mL). The organic layer was dried (Na<sub>2</sub>SO<sub>4</sub>), filtered and evaporated to dryness. The final residue was purified by flash column chromatography on silica gel (Hexane/ethyl acetate 3:1 to 1:2) to give 94 mg (67%) of **7b** as a white solid. Spectroscopic data are included in the Supplementary Material. MS (ESI, positive mode) *m/z*: 785.73 (M + 1)<sup>+</sup>.

#### 4.1.18. 4-(4-(((Benzyloxy)carbonyl)amino)butyl)-1-(3-(2-(1-((benzyloxy)carbonyl)piperidin-4-yl)ethoxy)-4-(4-phenethylthiazol-2-yl)phenyl)-3-methyl-1H-1,2,3-triazol-3-ium trifluoromethanesulfonate (**8a**)

Triazole **7a** (90 mg, 0.11 mmol) dissolved in anhydrous CH<sub>2</sub>Cl<sub>2</sub> (13 mL) was reacted with methyl trifluoromethanesulfonate (13  $\mu$ L, 0.11 mmol) at room temperature for 15 min under argon atmosphere, following the general *N*-alkylation procedure mentioned above. After the work-up, the final residue was purified by CCTLC on the Chromatotron (CH<sub>2</sub>Cl<sub>2</sub>/MeOH, 95:5) to obtain 85 mg (80%) of **8a** as a yellow oil. Spectroscopic data are included in the Supplementary Material. HRMS (ES, positive mode) *m/z*: calculated for C<sub>47</sub>H<sub>53</sub>N<sub>6</sub>O<sub>5</sub>S 813.3798; found 813.3810 (1.44 ppm).

#### 4.1.19. 4-(4-(((Benzyloxy)carbonyl)amino)butyl)-1-(3-(1-((benzyloxy)carbonyl)piperidin-4-yl)methoxy)-4-(4-phenethylthiazol-2-yl)phenyl)-3-methyl-1H-1,2,3-triazol-3-ium trifluoromethanesulfonate (**8b**)

According to the general *N*-alkylation procedure of triazoles, a solution of **7b** (160 mg, 0.2 mmol) in dry CH<sub>2</sub>Cl<sub>2</sub> (20 mL) was reacted with methyl trifluoromethanesulfonate (22.6  $\mu$ L, 0.2 mmol). After the work-up, the solvent was removed in vacuum and the final residue was purified by CCTLC on the Chromatotron (CH<sub>2</sub>Cl<sub>2</sub>/MeOH from 100:2 to

100:6). The fastest moving fractions afforded 53 mg (33%) of unreacted starting material. The slowest moving band afforded 96 mg (50%) of **8b** as a white solid. Spectroscopic data are included in the Supplementary Material. MS (ESI, positive mode) *m/z*: 799.74 (M + 1)<sup>+</sup>.

#### 4.1.20. (4-(2-(5-(4-(4-Ammoniobutyl)-3-methyl-1H-1,2,3-triazol-3-ium-1-yl)-2-(4-phenethylthiazol-2-yl)phenoxy)ethyl)piperidin-1-ium) di (2,2,2-trifluoroacetate) trifluoromethanesulfonate (**9a**)

A solution of protected triazolium salt **8a** (80 mg, 0.08 mmol) in a 1:1 mixture of THF/MeOH (20 mL) was reacted with Pd/C 10% (16 mg) and TFA (0.6 mL) at room temperature overnight, according to the general *N*-Cbz deprotection procedure mentioned above. After the work-up, the final residue was purified by reverse phase HPFC on a Biotage to yield 26 mg (34%) of **9a** as a yellow oil. Spectroscopic data are included in the Supplementary Material. HRMS (ES, positive mode) *m/z*: calculated for C<sub>31</sub>H<sub>41</sub>N<sub>6</sub>OS 545.3063; found 545.3067 (0.85 ppm); Anal. Calc. for C<sub>31</sub>H<sub>41</sub>N<sub>6</sub>OS.2TFA.TFO: C. 46.85; H. 4.70; N. 9.11; S. 6.95; found: C. 46.53; H. 4.69; N. 8.69; S. 6.69.

#### 4.1.21. 4-(4-Aminobutyl)-3-methyl-1-(4-(4-phenethylthiazol-2-yl)-3-(piperidin-4-ylmethoxy)phenyl)-1H-1,2,3-triazol-3-ium di (2,2,2-trifluoroacetate) trifluoromethanesulfonate (**9b**)

Following the general *N*-Cbz deprotection procedure, a solution of protected triazolium salt **8b** (115 mg, 0.12 mmol) in a 1:1 mixture of THF/MeOH (30 mL) containing Pd/C (10%) (20% wt/wt) was hydrogenated at room temperature for 2 h at atmospheric pressure. After the work-up, the final residue was purified by reverse phase HPFC on a Biotage to give 22 mg (21%) of **9b** as a yellow oil. Spectroscopic data are included in the Supplementary Material. HPLC (Gradient A, Agilent): *R*<sub>t</sub> = 6.59; HRMS (ES, positive mode) *m/z*: calculated for C<sub>30</sub>H<sub>39</sub>N<sub>6</sub>OS 531.2901; found 731.2923 (2.24 ppm).

#### 4.1.22. Experimental aqueous thermodynamic solubility studies

The water-solubility of the most representative parent triazole- and triazolium salt-based compounds **1a-d** and **4a-d** was determined by HPLC analysis. The HPLC runs were carried out on a Waters 484 System using Novapak C18 reverse phase column. Flow rate: 1 mL/min. Detection: UV 254 nm. Gradient solvent system A/B (acetonitrile/water): initial 10% A + 90% B; 10 min linear gradient to 100% B; Excess amount of the compounds was suspended in deionized water (pH = 5.5), sonicated for 10 min at room temperature, and then equilibrated overnight at room temperature. The samples were centrifuged at 14,000 rpm in a Hettich eppendorf microcentrifuge for 15 min at room temperature. An aliquot of the clear supernatant was removed and diluted to a concentration within the range of a five-point standard curve. Concentration of the five aqueous calibrations standards was 10  $\mu$ M, 50  $\mu$ M, 100  $\mu$ M, 250  $\mu$ M and 500  $\mu$ M, respectively. Water solubility was calculated by HPLC analysis by comparing the peak areas of each compound with those of standard solutions of the compounds in DMSO with a known concentration.

#### 4.2. Crystal structure of LiTryR complexed with compounds **4a** and **9a**

The LiTryR sample used for crystallization was concentrated to 7.5 mg/mL in 20 mM Tris-HCl buffer, pH 8. Native protein crystals were obtained by the hanging drop vapor diffusion method, mixing 1  $\mu$ L of protein sample with 1  $\mu$ L of well solution (0.1 M Tris-HCl, pH 8, 2.2 M (NH<sub>4</sub>)<sub>2</sub>SO<sub>4</sub>, 500  $\mu$ L reservoir volume). Yellow bipyramidal crystals grew within 2 days and were then used for different soaking experiments.

In order to obtain the structures of LiTryR in complex with the different ligands, native protein crystals were soaked for specific times in a compound-containing solution with similar composition to the crystallization condition. The TRL concentrations and soaking times used for the here solved crystal structures were as follows: LiTryR:**4a** complex 1 mM ligand and 40 min soaking; LiTryR:**9a** complex 1.5 mM ligand and 30 min soaking. Crystals were cryoprotected using a modified

reservoir solution supplemented with 25% glycerol and corresponding ligand prior to mounting and flash-freezing them into liquid nitrogen.

Single wavelength ( $\lambda = 0.979 \text{ \AA}$ ) diffraction data sets were collected at beamline BL13 (XALOC) of the ALBA Synchrotron (Barcelona, Spain) at 100 K. The XDS [59] program was used for indexing images and integration. CCP4 [60] programs AIMLESS [61] and MOLREP [62] were used for scaling and merging the data and molecular replacement, respectively. Five percent of the diffraction data was reserved for cross-validation and the *LiTryR* structure (PDB ID: 2JK6) as the search model. One monomer was found in the asymmetric unit and its structure was refined using REFMAC [63] employing tight geometric restraints, jelly body refinement, and map sharpening. Manual model building was carried out using the program COOT [64]. Crystal parameters, data collection, and relevant statistics are listed in Table 3.

### 4.3. Biological methods

#### 4.3.1. Chemical compounds and reagents

Stock solutions of synthesized compounds were prepared in anhydrous DMSO (Sigma-Aldrich, Saint Louis, MO) at 15 mM and stored at  $-20 \text{ }^\circ\text{C}$ .

All reagents for the *in vitro* enzymatic and *in cellulo* activity assays were obtained from Sigma-Aldrich (Saint Louis, MO) except for TS<sub>2</sub>, RPMI-1640 with L-glutamine and M199 mediums, which were purchased from Bachem (Bubendorf, Switzerland), Lonza (Basel, Switzerland) and Gibco (Leiden, The Netherlands), respectively.

#### 4.3.2. *LiTryR* purification

HIS-FLAG-tagged and HIS-tagged versions of recombinant *Leishmania infantum* TryR (*LiTryR*) were used for the dimer quantitation and the oxidoreductase activity assays, respectively. Both *LiTryR* versions were purified from *Escherichia coli* as already described [25]. Briefly, the HIS-FLAG-tagged *LiTryR* heterodimer was purified from BL21 (DE3) Rossetta *E. coli* transformed with *pET24a-FLAG-LiTryR* and *pRSETA-HIS-LiTryR* constructs, while the HIS-tagged *LiTryR* homodimer were purified from the same *E. coli* strain transformed with *pRSETA-HIS-LiTryR* construct alone. Overnight *E. coli* cultures grown at  $37 \text{ }^\circ\text{C}$  in LB medium with suitable antibiotics and vigorous shaking were used to inoculate (1:100) fresh LB medium supplemented with the same antibiotics. Scaled-up *E. coli* cultures were allowed to grow in the same conditions until a OD<sub>600</sub> of 0.5 was reached. *LiTryR* expression was induced upon addition of 1 mM isopropyl- $\beta$ -D-1-thiogalactopyranoside (Thermo Scientific, Waltham, MA) during 16 h at  $26 \text{ }^\circ\text{C}$ . Cells were harvested by centrifugation at 9,000g and  $4 \text{ }^\circ\text{C}$  and the wet pellets were resuspended in buffer A (50 mM Tris pH 7, 300 mM NaCl) containing 25 mM imidazole, a protease inhibitor cocktail and 1 mg/mL lysozyme. After a 30 min incubation on ice, the cell lysate was disrupted by sonication on ice (50% pulses, potency 7) for 30 min using a Sonifier Cell Disruptor B15 (Branson, Danbury, CT, USA) and centrifuged during 1 h at 50,000g and  $4 \text{ }^\circ\text{C}$ . Supernatant was collected and sonicated again as previously described for additional 10 min. The clarified supernatant containing soluble proteins was loaded onto a HisTrap column (GE Healthcare, Chicago, IL, USA) for 16 h at  $4 \text{ }^\circ\text{C}$  using a peristaltic pump P-1 (GE Healthcare, Chicago, IL, USA). The HisTrap column was subsequently connected to an AKTA purifier UPC 10 (GE Healthcare, Chicago, IL, USA) and extensively washed using 25 mL of a 10% fixed gradient between buffers A and B (50 mM Tris pH 7, 300 mM NaCl and 500 mM imidazole). HIS-FLAG-tagged *LiTryR* heterodimers and/or HIS-tagged *LiTryR* homodimers were isocratically eluted using a 40% fixed gradient between buffers A and B. Fractions containing recombinant *LiTryR* were pooled and loaded onto a HiPrep™ 26/10 Desalting column (GE Healthcare, Chicago, IL, USA) previously equilibrated with buffer A to remove imidazole. Protein concentration was determined using the theoretical values for the molar extinction coefficient and molecular weight of the different *LiTryR* versions using a NanoDrop™ spectrophotometer (Thermo Scientific, Waltham, MA). Finally, *LiTryR*

was concentrated to 2 mg/mL using an Amicon® Ultra-15 50K (Merck Millipore, Burlington, MA, USA) and an equal volume of glycerol was added before storing at  $-20 \text{ }^\circ\text{C}$ .

For *LiTryR* crystallization, the coding sequence of *LiTryR* was cloned into pET28a plasmid. The recognition sequence of PreScission protease was also introduced in this construct to cleave the N-terminal HIS tag. Induction of protein expression was carried out for 4 h at  $37 \text{ }^\circ\text{C}$ . Protein purification was performed with a slightly modified version of the protocol explained above. Following buffer exchanging in the HiPrep™ 26/10 Desalting column (GE Healthcare, Chicago, IL, USA), an anion exchange chromatography was performed using a HiTrap™ Q High Performance column. Fractions containing recombinant *LiTryR* were pooled and digested with GST-PreScission protease in a 1:30 ratio (protease:*LiTryR*) for 16 h at  $4 \text{ }^\circ\text{C}$ . PreScission-digested *LiTryR* was loaded onto a GSTrap™ connected in series to a HisTrap™ Fast Flow columns (GE Healthcare, Chicago, IL, USA) for 16 h at  $4 \text{ }^\circ\text{C}$  using a peristaltic pump P-1 (GE Healthcare, Chicago, IL, USA). *LiTryR* was recovered from the flow-through, and GST-PreScission protease and the histidine tails cleaved from *LiTryR* remained bound to the GSTrap and the HisTrap, respectively. Finally, *LiTryR* was concentrated to 15 mg/mL using an Amicon® Ultra-15 50K (Merck Millipore, Burlington, MA, USA) and stored at  $4 \text{ }^\circ\text{C}$ .

#### 4.3.3. *TbTryR*, *TcTryR* and *TcoTryR* purification

The complete DNA coding sequences of *T. brucei* TryR (*TbTryR*), *T. cruzi* TryR (*TcTryR*) and *T. congolense* TryR (*TcoTryR*) were PCR-amplified and cloned in the pRSETA plasmid. Genomic DNA from *T. brucei* S16 cell line was kindly provided by Dr. José M. Pérez-Victoria (Instituto de Parasitología y Biomedicina "López - Neyra"-CSIC, Granada, Spain). Genomic DNA from *T. cruzi* Brener cell line was kindly provided by Dr. Manuel C. López-López (Instituto de Parasitología y Biomedicina "López - Neyra"-CSIC, Granada, Spain). Genomic DNA from *T. congolense* parasites was kindly provided by Dr. Stefan Magez (Vrije Universiteit Brussel, Brussels, Belgium). HIS-tagged versions of recombinant *T. brucei*, *T. cruzi* and *T. congolense* TryRs were purified from *E. coli* as already explained for the HIS-tagged version of recombinant *LiTryR*.

#### 4.3.4. hGR purification

Recombinant HIS-tagged version of the cytoplasmic isoform of human GR (lacking the first 43 amino acids corresponding to the mitochondrial signal peptide) was PCR-amplified and cloned in the pRSETA plasmid. The DNA coding for *Homo sapiens* GR (transcript variant 1; NCBI Reference Sequence: NM\_000637.5) was purchased from GeneScript. HIS-tagged version of recombinant hGR was purified from *E. coli* as already explained for the HIS-tagged version of recombinant *LiTryR* but inducing protein expression at  $37 \text{ }^\circ\text{C}$  instead of  $26 \text{ }^\circ\text{C}$ .

#### 4.3.5. TryR oxidoreductase activity

TryR oxidoreductase activity was determined spectrophotometrically using a modified version of the 5,5'-dithiobis-2-nitrobenzoic acid (DTNB)-coupled assay described by Hamilton et al. [65]. For regular IC<sub>50</sub> determinations in *LiTryR*, reactions were conducted at  $26 \text{ }^\circ\text{C}$  in 250  $\mu\text{l}$  of a buffer containing 40 mM HEPES pH 7.5, 1 mM EDTA, 30  $\mu\text{M}$  NADP<sup>+</sup>, 25  $\mu\text{M}$  DTNB, 1  $\mu\text{M}$  TS<sub>2</sub>, 150  $\mu\text{M}$  NADPH, 0.02% glycerol, 1.75% DMSO and 7 nM recombinant *LiTryR*. For IC<sub>50</sub> determinations in different TryRs (including *LiTryR*, *TbTryR*, *TcTryR* and *TcoTryR*), TS<sub>2</sub> and TryR concentrations were adjusted to 50  $\mu\text{M}$  and 0.5 nM, respectively. DTNB, DMSO and glycerol concentrations used in this assay do not have any relevant effect on the kinetics of the TryR oxidoreductase reaction. Reactions were started by addition of a mixture of NADPH and TS<sub>2</sub>. TryR oxidoreductase activity was monitored at  $26 \text{ }^\circ\text{C}$  by the increase in absorbance at 412 nm due to TNB generation in an EnSpire Multimode Plate Reader (PerkinElmer, Waltham, MA).

TNB (2-nitro-5-thiobenzoic acid) concentration was calculated by multiplying the absorbance values by 100 (since 50  $\mu\text{M}$  TNB generates 0.5 arbitrary units of absorbance at 412 nm). As in other DTNB-coupled



assays, 1 mol of thiol reacts with 1 mol of DTNB producing 1 mol of TNB. Thus, in our case, one molecule of T(SH)<sub>2</sub> (containing two thiol groups) reduces one molecule of DTNB producing two molecules of TNB (each containing one thiol group). The initial rates of the reactions were estimated from the slope at the origin of the reaction progress curves. The initial velocities in the presence of different inhibitor concentrations (ranging from 0.1 to 75  $\mu$ M) were normalized as a percentage with respect to the initial velocity in the presence of the inhibitor vehicle (DMSO). IC<sub>50</sub> values for each compound were obtained by fitting these percentages to a nonlinear regression model with the GraFit 6 software (Erithacus, Horley, Surrey, UK). All the assays were conducted in three independent experiments.

#### 4.3.6. hGR oxidoreductase activity

hGR oxidoreductase activity was determined spectrophotometrically using a DTNB-coupled assay. Briefly, reactions were carried out at 37 °C in 250  $\mu$ l a buffer containing 40 mM HEPES pH 7.5, 1 mM EDTA, 30  $\mu$ M NADP<sup>+</sup>, 25  $\mu$ M DTNB, 50  $\mu$ M oxidized glutathione, 150  $\mu$ M NADPH, 0.02% glycerol, 1.75% DMSO and 5 nM recombinant hGR. DTNB, DMSO and glycerol concentrations used in this assay do not have any relevant effect on the kinetics of the hGR enzymatic reaction. Reactions were started by addition of a mixture of NADPH and oxidized glutathione. hGR oxidoreductase activity was monitored at 37 °C by the increase in absorbance at 412 nm due to TNB generation in an EnSpire Multimode Plate Reader (PerkinElmer, Waltham, MA).

Data were analyzed as explained above in the TryR oxidoreductase activity of the Experimental Section. All the assays were conducted in three independent experiments.

#### 4.3.7. Dimer quantitation assay

The ability of 1,2,3-triazolium salts to disrupt LiTryR homodimer was evaluated using an enzyme-linked immunosorbent assay (ELISA) developed in our laboratory [25]. Briefly, 400 nM HIS-FLAG-tagged LiTryR was incubated in 1.5 mL microcentrifuge tubes with different compounds (ranging from 3.1 to 75  $\mu$ M) in dimerization buffer (50 mM Tris pH 8.0 and 300 mM NaCl) for 16 h at 37 °C with vigorous shaking and in a humid atmosphere (1 mL/tube). The different solutions were subsequently centrifuged at 18,000 $\times$ g for 15 min at room temperature. Supernatants were added to 96-well  $\alpha$ -FLAG-coated plates (200  $\mu$ L/well) and incubated for 30 min at 37 °C in a humid atmosphere with vigorous shaking. The plates were washed five times with TTBS buffer (200  $\mu$ L/well of 2 mM Tris pH 7.6, 138 mM NaCl and 0.1% Tween-20) and incubated with diluted monoclonal  $\alpha$ -HIS antibody conjugated to horseradish peroxidase (1:50,000; Abcam, Cambridge, UK) in TTBS buffer containing 5% fatty acid- and essentially globulin-free bovine serum albumin (200  $\mu$ L/well) for 1 h at room temperature. The plates were washed again five times with TTBS buffer, and o-phenylenediamine dihydrochloride substrate, prepared according to the manufacturer's instructions, was added (100  $\mu$ L/well). The enzymatic reaction of horseradish peroxidase was stopped after 5 min with 0.5 M H<sub>2</sub>SO<sub>4</sub> (100  $\mu$ L/well), and the absorbances were measured at 490 nm in an EnSpire Multimode Plate Reader (PerkinElmer, Waltham, MA).

For IC<sub>50</sub> determinations, the absorbance values in the presence of different concentrations of inhibitor were normalized as a percentage with respect to the absorbance value in the presence of DMSO. IC<sub>50</sub> values for each compound were obtained by fitting these percentages to a nonlinear regression model with the GraFit 6 software (Erithacus, Horley, Surrey, UK). All the assays were conducted in triplicate in three independent experiments.

#### 4.3.8. Determination of inhibitory constants

The inhibitory constants were calculated following a slightly modified version of the standard DTNB-coupled assay explained above. TS<sub>2</sub> was serially diluted in a buffer containing 40 mM HEPES pH 7.5 and 1 mM EDTA (6-fold dilution from 1666 to 52  $\mu$ M). The different TS<sub>2</sub> solutions were dispensed into a 96-well microplate (15  $\mu$ L/well).

Inhibitors were serially diluted in DMSO. The different aliquots of the inhibitor dilutions and the equivalent amount of the vehicle (DMSO) were added to a pre-assay mixture yielding different mixtures containing 40 mM HEPES pH 7.5, 1 mM EDTA, 416.67  $\mu$ M NADPH, 208.33  $\mu$ M DTNB, 1.45% DMSO and different inhibitor concentrations. These mixtures were subsequently added to the appropriate wells previously filled with different TS<sub>2</sub> solutions (180  $\mu$ L/well). The assay was initiated upon addition of 55  $\mu$ L of a buffer containing 40 mM HEPES pH 7.5, 1 mM EDTA, 272.73  $\mu$ M NADP<sup>+</sup>, 0.01% glycerol and 2.3 nM recombinant LiTryR using an automated dispensing system (PerkinElmer, Waltham, MA). Coupling an automated dispenser unit to the spectrophotometer allowed real-time detection of the enzymatic reaction, which was critical for obtaining high quality fits of the experimental data and, especially, to estimate the initial velocity of the reaction progress curves. The order of addition of the different solutions was critical to avoid enzyme preincubation with the inhibitor or the substrates. The final 250  $\mu$ L assay contained 40 mM HEPES buffer pH 7.5, 1 mM EDTA, 300  $\mu$ M NADPH, 60  $\mu$ M NADP<sup>+</sup>, 150  $\mu$ M DTNB, 3.1–100  $\mu$ M TS<sub>2</sub>, 1.04% DMSO, 0.002% glycerol and 0.5 nM recombinant LiTryR. The oxidoreductase activity was monitored at 26 °C by the increase in absorbance at 412 nm in an EnSpire Multimode Plate Reader (PerkinElmer, Waltham, MA). All the assays were conducted in three independent experiments.

#### 4.3.9. Leishmania cell lines and culture

*L. infantum* promastigotes (MCAN/ES/89/IPZ229/1/89) were grown in RPMI-1640 with L-glutamine medium supplemented with 10% heat-inactivated fetal calf serum (FCS), 100  $\mu$ g/mL streptomycin and 100 units/mL penicillin (Gibco, Leiden, The Netherlands), and 25 mM HEPES pH 7.2 at 26 °C. *L. infantum* axenic amastigotes (MCAN/ES/89/IPZ229/1/89) were grown in M199 medium supplemented with 10% heat-inactivated FCS, 100  $\mu$ g/mL streptomycin and 100 units/mL penicillin (Gibco, Leiden, The Netherlands), 10 mg/L gentamicin, 100 mg/L L-asparagine, 1 g/L  $\beta$ -alanine, 50 mg/L sodium pyruvate, 200 mg/L sucrose, 320 mg/L malic acid, 40 mg/L fumaric acid, 70 mg/L succinic acid, 200 mg/L  $\alpha$ -ketoglutaric acid, 300 mg/L citric acid, 0.4 mg/L hemin, 1.1 g/L sodium bicarbonate, and 5 g/L MES pH 5.4 at 37 °C.

#### 4.3.10. Axenization of *L. infantum* promastigotes

Axenization was performed by inoculating 0.5 mL of a 7-day stationary phase culture of *L. infantum* promastigotes (approximately  $\sim$ 2-3 $\times$ 10<sup>7</sup> parasites/mL) in 4.5 mL of amastigotes medium and incubating the culture at 37 °C for 3 days. Axenization of *L. infantum* promastigotes was followed by phase-contrast microscopy in an Eclipse Ti inverted microscope (Nikon, Tokyo, Japan).

#### 4.3.11. Leishmanicidal activity

*L. infantum* axenic amastigotes from logarithmic cultures were seeded at a concentration of 10<sup>5</sup> parasites/mL (1 mL/well) in 96-well Nunclon™ Delta Surface microplates (Nunc, Roskilde, Denmark). Drug treatments were subsequently performed for 24 h at 37 °C. Microplates were sealed with parafilm during all the incubation periods.

Parasite viability was evaluated by flow cytometry using the propidium iodide (PI) exclusion method. Briefly, *L. infantum* axenic amastigotes were stained for 10 min with 10  $\mu$ g/mL PI and subsequently acquired by a Cytomics FC500 MCP flow cytometer (Beckman Coulter, Brea, CA). Each sample was acquired for 10 s (50  $\mu$ L/well).

Data were analyzed using the CXP software (Beckman Coulter, Brea, CA). Briefly, after selecting *L. infantum* amastigotes population based on their side scatter (SSC) and forward scatter (FSC) values, live and dead parasite cells were recognized by their permeability to PI. For EC<sub>50</sub> determinations, the percentage of live parasites was calculated by normalizing the mean of the total number of live parasites at each condition to the mean of the vehicle-treated controls. EC<sub>50</sub> values for each compound were obtained by fitting these percentages to a nonlinear regression model with the GraFit 6 software (Erithacus, Horley, Surrey, UK). All the assays were performed in triplicate in three

independent experiments.

#### 4.3.12. Human cell lines culture

THP-1 cells were grown in RPMI-1640 medium with L-glutamine supplemented with 10% heat inactivated FCS, 100 µg/mL streptomycin and 100 units/mL penicillin (Gibco, Leiden, The Netherlands), 1 mM sodium pyruvate, and 10 mM HEPES pH 7.5 at 37 °C and 5% CO<sub>2</sub>.

Liver hepatocellular carcinoma HepG2 cells were grown in DMEM medium supplemented with 10% heat inactivated FCS, 100 µg/mL streptomycin and 100 units/mL penicillin (Gibco, Leiden, The Netherlands), and 10 mM HEPES pH 7.5 at 37 °C and 5% CO<sub>2</sub>.

#### 4.3.13. In vitro infection of THP-1 derived macrophages with GFP-expressing *L. infantum* axenic amastigotes

THP-1 monocytes were seeded in 48-well Nunclon™ Delta Surface microplates (Nunc, Roskilde, Denmark) at a concentration of  $5 \times 10^5$  cells/mL in RPMI complete medium supplemented with 100 ng/mL phorbol 12-myristate 13-acetate (PMA) (250 µL/well). PMA-differentiation of THP-1 monocytes to macrophages was allowed for 24 h at 37 °C and 5% CO<sub>2</sub>. THP-1 derived macrophages were infected with GFP-expressing *L. infantum* axenic amastigotes at  $5 \times 10^6$  parasites/mL in RPMI-1640 complete medium for 24 h (250 µL/well). Non-internalized amastigotes were washed out twice with PBS (250 µL/well). The remaining non-internalized parasites were challenged for 24 h with THP-1 medium supplemented with 10% horse serum (Gibco, Leiden, The Netherlands) instead of FCS (250 µL/well). Extracellular dead parasites were removed by aspiration and infected macrophages were washed twice with PBS (250 µL/well). Drug treatment of infected macrophages was performed in 500 µL of fresh RPMI-1640 medium supplemented with 10% horse serum. Following a 72-h incubation at 37 °C and 5% CO<sub>2</sub>, treatments were removed by two PBS washes (500 µL/well).

Cytotoxicity of THP-1 infected macrophages was determined using the resazurin/alar blue fluorometric assay. Briefly, AlamarBlue™ HS Cell Viability Reagent (Invitrogen, Leiden, The Netherlands) was prepared in RPMI-1640 complete medium according to the manufacturer's instructions and subsequently added to the 48-well microplates (150 µL/well). After a 2 h-incubation at 37 °C and 5% CO<sub>2</sub>, the color of the cell culture medium gradually changed from blue to pink due to intracellular enzymatic reduction of resazurin into resorufin, which is subsequently excreted into the medium. The cell culture media were transferred (100 µL/well) to black opaque 96-well microplates (PerkinElmer, Waltham, MA). Fluorescence due to resorufin production was measured at an emission wavelength of 590 nm using an excitation wavelength of 560 nm in an EnSpire Multimode Plate Reader (PerkinElmer, Waltham, MA).

The excess of resazurin was aspirated from the 48-well microplates and the infected macrophages were washed once with PBS (500 µL/well). Lysis of infected macrophages was performed with 120 µL of SDS 0.005% (w/v) in PBS. After a 30 min incubation at 37 °C and 5% CO<sub>2</sub>, the lysis was stopped upon addition of RPMI complete medium with 20 µg/mL PI (120 µL/well). The cell lysates were transferred to a 96-well microplate (200 µL/well) and the GFP<sup>+</sup> amastigotes extracted from the infected macrophages were acquired by a Cytomics FC500 MCP flow cytometer (Beckman Coulter, Brea, CA). Each sample was acquired for 20 s (100 µL/well).

For half-maximal cytotoxic concentration (CC<sub>50</sub>) determinations, the percentage of live and infected macrophages was estimated by normalizing the resorufin fluorescence values obtained at each treatment condition to the value of the vehicle-treated controls. CC<sub>50</sub> values for each compound were obtained by fitting these percentages to a nonlinear regression model with the GraFit 6 software (Erithacus, Horley, Surrey, UK).

For determining the EC<sub>50</sub> values in *L. infantum* intracellular amastigotes, the relative number of GFP<sup>+</sup> intracellular amastigotes per macrophage in each sample was estimated by dividing the total number of GFP<sup>+</sup> amastigotes by the corresponding resorufin fluorescence value.

Results were then normalized to the vehicle-treated controls. EC<sub>50</sub> values for each compound were obtained by fitting these normalized results to a nonlinear regression model with the GraFit 6 software (Erithacus, Horley, Surrey, UK). All the assays were conducted in three independent experiments.

#### 4.3.14. Determination of cellular toxicity

Liver hepatocellular carcinoma HepG2 cells were seeded in 24-well Nunclon™ Delta Surface microplates (Nunc, Roskilde, Denmark) at a concentration of  $10^5$  cells/mL at 37 °C and 5% CO<sub>2</sub> in DMEM complete medium and allowed to attach to the cell culture-treated surface of the microplates for 24 h. Drug treatment of HepG2 cells was performed during the logarithmic growth phase at 37 °C and 5% CO<sub>2</sub> for 24 h in DMEM complete medium to compare the cytotoxic effect of the compounds against HepG2 cells and *L. infantum* axenic amastigotes. Drug treatment of HepG2 cells was performed during the logarithmic growth phase at 37 °C and 5% CO<sub>2</sub> for 72 h in DMEM medium supplemented with 10% horse serum to compare the cytotoxic effect of the compounds against HepG2 cells and *L. infantum* intracellular amastigotes. As performed in the infection experiments detailed above, DMEM medium was supplemented with 10% horse serum instead of 10% heat-inactivated FCS to compensate for any difference in terms of compound retention.

The cytotoxic activity of the compounds was evaluated by the crystal violet assay. Briefly, cells were washed with PBS and stained with crystal violet solution (0.2% crystal violet, 2% ethanol) for 10 min at room temperature (200 µL/well). The microplates were subsequently washed twice with tap water and allowed to dry. Finally, the stained cells were solubilized with 1% SDS (400 µL/well), and color intensity was quantified at 570 nm using an EnSpire Multimode Plate Reader (PerkinElmer, Waltham, MA).

For CC<sub>50</sub> determinations, the percentage of live HepG2 cells was estimated by normalizing the absorbance values obtained at each treatment condition to the value of the vehicle-treated controls. CC<sub>50</sub> values for each compound were obtained by fitting these percentages to a nonlinear regression model with the GraFit 6 software (Erithacus, Horley, Surrey, UK). All the assays were conducted in three independent experiments.

#### 4.3.15. Determination of non-protein thiols in *L. infantum* promastigotes

*L. infantum* promastigotes from logarithmic cultures were seeded at a concentration of  $2 \times 10^6$  parasites/mL (1 mL/well) in 24-well Nunclon™ Delta Surface microplates (Nunc, Roskilde, Denmark) and treated with the vehicle of the treatments, 625 µM H<sub>2</sub>O<sub>2</sub> and/or 75 µM compound 4c for 1 h. Microplates were sealed with parafilm during all the incubation periods. 100 nM of the fluorescent probe 5-chloromethylfluorescein diacetate (CMFDA; Invitrogen, Leiden, The Netherlands) was added 30 min before the end of the treatment. CMFDA is a non-fluorescent molecule that penetrates cells where its acetate groups are cleaved by intracellular esterases, releasing 5-chloromethylfluorescein (CMF). CMF is a fluorescent molecule that interacts with the thiol groups through its chloromethyl group, thus forming very stable and impermeable conjugates. Following the 1 h incubation, parasites were transferred to 1.5 mL microcentrifuge tubes, centrifuged at 1,000g and washed twice with PBS (1 mL/tube) to remove the excess of non-internalized CMFDA. *L. infantum* promastigotes resuspended in 250 µL of PBS were transferred to a 96-well microplate and stained for 10 min with 10 µg/mL PI. Samples were acquired by a Cytomics FC500 MCP flow cytometer (Beckman Coulter, Brea, CA). The population of live promastigotes was selected based on SSC and FSC values, and their PI exclusion. 10<sup>4</sup> events/sample belonging to this population were acquired and the fluorescence intensity due to the 5-chloromethylfluorescein conjugates with non-protein thiol groups was recorded. Data were analyzed using the CXP software (Beckman Coulter, Brea, CA).

#### 4.3.16. Data and statistical analysis

All linear and nonlinear regressions were performed using GraFit 6.0

software (Erithacus, Horley, SRY, UK) All experiments were repeated at least three times to ensure the reliability of single values.

$v_i$ ,  $v_s$ ,  $k_{obs}$  and  $d$  values were estimated for every **4c** concentration at all  $TS_2$  concentrations by fitting the values of TNB concentration produced during each enzymatic reaction to Equation (1) [44,45,50]:

$$[P] = v_s t + \frac{v_i - v_s}{k_{obs}} [1 - \exp(-k_{obs}t)] + d \quad (1)$$

where  $t$  is the reaction time,  $v_i$  and  $v_s$  are the initial and the steady-state rates, respectively,  $k_{obs}$  is the apparent first-order rate constant for establishing the steady-state equilibrium between EI and E\*I and  $d$  is the displacement of the curve from the vertical ordinate and accounts for any nonzero value of the measured absorbance at time zero caused by some of the reagents. To ensure the linearity of the enzymatic reaction in the absence of inhibitor due to  $TS_2$  depletion, the analysis was performed with experimental data obtained during the first 15,000 s to avoid  $TS_2$  depletion. Under this condition, all uninhibited reactions showed straight lines until the generation of 230  $\mu$ M TNB. This product concentration was never reached in the inhibited reactions during the first 15,000 s.

The apparent inhibition constants  $K_i^{app}$  and  $K_i^{*app}$  for each  $TS_2$  concentration were determined, by nonlinear regression, fitting the values obtained at different **4c** concentrations for  $v_i$  or  $v_s$ , respectively, to Equation (2) and Equation (3) [45]:

$$\frac{v_i}{v_o} = \frac{1}{1 + \frac{[I]}{K_i^{app}}} \quad (2)$$

$$\frac{v_s}{v_o} = \frac{1}{1 + \frac{[I]}{K_i^{*app}}} \quad (3)$$

where  $v_o$  is the velocity of the uninhibited reaction,  $K_i^{app}$  is the apparent value of the  $K_i$  for the initial encounter complex (EI) at a given  $TS_2$  concentration and  $K_i^{*app}$  is the apparent value of the overall steady-state dissociation constant ( $K_i^*$ ) at a given  $TS_2$  concentration.

The  $K_i$  value for the dissociation of the initial EI complex was determined by fitting the  $K_i^{app}$  values obtained at different  $TS_2$  concentrations to Equation (4) [44,45]. In addition, this graph was used to assess the inhibition modality of **4c** during the first rapid equilibrium of its two-step binding mechanism. The value obtained for  $\alpha$  defines the mode of inhibition (competitive:  $\alpha \rightarrow$  infinite; uncompetitive:  $\alpha \rightarrow 0$ ; pure noncompetitive  $\alpha = 1$ ; mixed:  $1 < \alpha < 10$ ).

$$K_i^{app} = \frac{[S] + k_m}{\frac{k_m}{K_i} + \frac{[S]}{\alpha k_i}} \quad (4)$$

The value for the overall steady-state dissociation constant ( $K_i^*$ ) was determined by fitting the  $K_i^{*app}$  values obtained at different  $TS_2$  concentrations to Equation (5) [44,45]. In addition, this graph was used to assess the overall inhibition modality of **4c** during its two-step binding mechanism. As explained above, the value obtained for  $\alpha$  defines the mode of inhibition.

$$K_i^{*app} = \frac{[S] + k_m}{\frac{k_m}{K_i} + \frac{[S]}{\alpha k_i^*}} \quad (5)$$

For the statistical analysis of non-protein thiol determinations in *L. infantum*, standardized kurtosis was analyzed to determine whether the samples come from normal distributions. To ensure normality, values of these statistics were always tested to be within the range of  $-2$  to  $+2$ . Once the normal distribution of data was checked, the Excel T. Test function with the specific parameters for a two tailed analysis of heteroskedastic independent samples was used to compute P-values and decide if the null hypothesis (mean 1 = mean 2) can be rejected.

#### 4.4. Screening for pan-assay interference compounds and aggregation

All tested compounds were screened *in silico* for pan-assay interference compounds (PAINS) and aggregation. SMILES representations were generated and passed through two public PAINS filters available in ZINC (<http://zinc15.docking.org/patterns/home/>) and CBLigand (<http://www.cbligand.org/PAINS/>). None of the compounds' sub-structures were identified as PAINS or aggregators. Dose-response curves for all experiments and compounds were recorded. None of the curves displayed steep Hill slopes that could be an indication for PAINS (dose-response curves for representative compounds **4b** and **4c** are presented in Fig. S10, Supplementary Material). Counter-screening against related (hGR) and unrelated (*E. coli* AmpC  $\beta$ -lactamase and *L. infantum* superoxide dismutase A) drug targets discarded any non-specific activity of the compounds. Reaction progress curves for *LiTryR* and hGR in the presence of representative compounds **4b** and **4c** are shown in Fig. S11. Nifurtimox is included as a well-known inhibitor of hGR. SAR, considered the most relevant criterion that discriminates PAINS and non-PAINS is deeply discussed in the manuscript.

#### 4.5. Computational methods

##### 4.5.1. Unrestrained MD simulations

The crystal structures of *LiTryR* in complex with **4a** or **9a** bound at the active site (PDB ids. 6T95 and 6T98, respectively) were employed as initial coordinates for the unrestrained MD simulations in water, which were run using the AMBER force field and the AMBER suite of programs as described before for the pyrrolopyrimidine [49] and triazole series [27]. The molecular graphics program PyMOL [66] was employed for molecular editing (e.g., conversion of **4a** to **4c**), visualization, and figure preparation. The binding energy analyses were carried out with our in-house tool MM-ISMSA [67].

##### 4.5.2. Steered MD simulations

RESP charges for **4a** and **4c** were obtained from computing the electrostatic potential on their optimized geometries (HF/6-31G\*//BP86-D3/def2svp). The rest of the system was described with the Amber19SB force field [68]. The complexes of *LiTryR*:**4a** and *LiTryR*:**4c** complexes were solvated with a box of OPC water molecules [69], neutralized with 24  $Na^+$  ions, and energy-minimized in three consecutive steps: first hydrogens, then solvent molecules and counterions, and finally all atoms were allowed to relax. The final energy-minimized systems were heated from 100 to 300 K over 1 ns using the Langevin thermostat and keeping the volume constant (NVT ensemble). A cutoff of 10 Å was defined for the direct calculation of the electrostatic term. The solute (protein, cofactors and **4a/4c**) were not allowed to move during the heating phase by imposing a harmonic constraint to each atom of 200 kcal.mol<sup>-1</sup>Å<sup>-2</sup>. Thereafter, this constraint was gradually removed in 5 steps of 20 ps each at 300 K and the system also switched from NVT to NPT (constant pressure) conditions. The resulting solvated complexes were then used as initial geometries for the steered MD simulations (sMD). To bring **4a** or **4c** into the interfacial cavity, the distance between the center of mass of either the phenyl group (**4a**) or the biphenyl group (**4c**) and the center of the triangle formed by residues Gly431A, Thr463A and Thr65B (located inside the cavity) was defined as the reaction coordinate (RC). The sMD was run for 1 ns at 300 K and constant pressure. A total of 500 points separated by 2 ps were saved to be used in the next step. All calculations were run with Amber20 [70] using the *pmemd.cuda* engine on a single GPU.

##### 4.5.3. Umbrella sampling MD simulations

Each of the former 500 snapshots was used as the initial geometry for MD simulations at 300 K and constant pressure, each lasting 10 ns, during which the initial coordinates were constrained with a harmonic constraint of 100 kcal.mol<sup>-1</sup>Å<sup>-2</sup> at the particular value of the previously

defined RC. By following this procedure, the system was allowed to relax at each window around the RC value. Care was taken to ensure that the oscillations around neighboring RC values overlapped between them along the whole RC. Finally, the energy profile was constructed using the program vFEP [71].

### Declaration of competing interest

The authors declare that they have no known competing financial interests or personal relationships that could have appeared to influence the work reported in this paper.

### Data availability

Data will be made available on request.

### Acknowledgements

This work has been financially supported by the Spanish MICINN (Projects PID2019-104070RB-C21, PID2019-104070RB-C22 and PID2020-115331 GB-I00), the Spanish Agencia Estatal Consejo Superior de Investigaciones Científicas (CSIC, Projects CSIC-PIE-201980E100 and CSIC-PIE-201980E028), and the Comunidad de Madrid (PLATESA2-CM ref. S-2018/BAA-4370). The Spanish MEC is also acknowledged for FPU grants to A. R. and to J.C.G. P.A.S.M. thanks to the Division of Physiological Chemistry and the Otto-Loewi Research Center of the Medical University of Graz for their support with the scientific cluster where the calculations contained in this work were run. We thank Ricardo Laureano-Rodríguez, Juan Antonio Rodríguez-Gutierrez, and Laura Lagartera for technical assistance with SPR experiments.

### Appendix. ASupplementary data

Supplementary data to this article can be found online at <https://doi.org/10.1016/j.ejmech.2022.114878>.

### References

- [1] Leishmaniasis, Available online: <https://www.who.int/news-room/fact-sheets/detail/leishmaniasis> (WHO).
- [2] S. Burza, S.L. Croft, M. Boelaert, Leishmaniasis, *Lancet* 392 (2018) 951–970.
- [3] P.M. Gillespie, C.M. Beaumier, U. Strych, T. Hayward, P.J. Hotez, M.E. Bottazzi, Status of vaccine research and development of vaccines for leishmaniasis, *Vaccine* 34 (2016) 2992–2995.
- [4] A.A. Bekhit, E. El-Agroudy, A. Helmy, T.M. Ibrahim, A. Shavandi, A.E.A. Bekhit, *Leishmania* treatment and prevention: natural and synthesized drugs, *Eur. J. Med. Chem.* 160 (2018) 229–244.
- [5] S. Hendrickx, G. Caljon, L. Maes, Need for sustainable approaches in antileishmanial drug discovery, *Parasitol. Res.* 118 (2019) 2743–2752.
- [6] N. Biyani, R. Madhubala, Quantitative proteomic profiling of the promastigotes and the intracellular amastigotes of *Leishmania donovani* isolates identifies novel proteins having a role in *Leishmania* differentiation and intracellular survival, *Biochim. Biophys. Acta* 1824 (2012) 1342–1350.
- [7] R.L. Krauth-Siegel, M.A. Comini, Redox control in trypanosomatids, parasitic protozoa with trypanothione-based thiol metabolism, *Biochim. Biophys. Acta* 1780 (2008) 1236–1248.
- [8] M. Dormeyer, N. Reckenfelderbaumer, H. Ludemann, R.L. Krauth-Siegel, Trypanothione-dependent synthesis of deoxyribonucleotides by *Trypanosoma brucei* ribonucleotide reductase, *J. Biol. Chem.* 276 (2001) 10602–10606.
- [9] D. Sela, N. Yaffe, J. Shlomai, Enzymatic mechanism controls redox-mediated protein-DNA interactions at the replication origin of kinetoplast DNA minicircles, *J. Biol. Chem.* 283 (2008) 32034–32044.
- [10] M.K. Mittal, S. Rai, Ravinder Ashutosh, S. Gupta, S. Sundar, N. Goyal, Characterization of natural antimony resistance in *Leishmania donovani* isolates, *Am. J. Trop. Med. Hyg.* 76 (2007) 681–688.
- [11] H. Castro, A.M. Tomas, Peroxidases of trypanosomatids, *Antioxidants Redox Signal.* 10 (2008) 1593–1606.
- [12] A. Ariza, T.J. Vickers, N. Greig, K.A. Armour, M.J. Dixon, I.M. Eggleston, A. H. Fairlamb, C.S. Bond, Specificity of the trypanothione-dependent *Leishmania major* glyoxalase I: structure and biochemical comparison with the human enzyme, *Mol. Microbiol.* 59 (2006) 1239–1248.
- [13] J. Tovar, S. Wilkinson, J.C. Mottram, A.H. Fairlamb, Evidence that trypanothione reductase is an essential enzyme in *Leishmania* by targeted replacement of the *tryA* gene locus, *Mol. Microbiol.* 29 (1998) 653–660.
- [14] J. Tovar, M.L. Cunningham, A.C. Smith, S.L. Croft, A.H. Fairlamb, Down-regulation of *Leishmania donovani* trypanothione reductase by heterologous expression of a trans-dominant mutant homologue: effect on parasite intracellular survival, *Proc. Natl. Acad. Sci. U.S.A.* 95 (1998) 5311–5316.
- [15] R.L. Krauth-Siegel, H. Bauer, R.H. Schirmer, Dithiol proteins as guardians of the intracellular redox milieu in parasites: old and new drug targets in trypanosomes and malaria-causing plasmodia, *Angew. Chem. Int. Ed.* 44 (2005) 690–715.
- [16] A.E. Leroux, R.L. Krauth-Siegel, Thiol redox biology of trypanosomatids and potential targets for chemotherapy, *Mol. Biochem. Parasitol.* 206 (2016) 67–74.
- [17] T. Battista, G. Colotti, A. Ilari, A. Fiorillo, Targeting trypanothione reductase, a key enzyme in the redox trypanosomatid metabolism, to develop new drugs against leishmaniasis and trypanosomiasis, *Molecules* 25 (2020) (1924).
- [18] F. Saccoliti, R. Di Santo, R. Costi, Recent advancement in the search of innovative antiprotozoal agents targeting trypanothione metabolism, *ChemMedChem* 15 (2020) 2420–2435.
- [19] A.H. Fairlamb, P. Blackburn, P. Ulrich, B.T. Chait, A. Cerami, Trypanothione: a novel bis(glutathionyl)spermidine cofactor for glutathione reductase in trypanosomatids, *Science* 227 (1985) 1485–1487.
- [20] S.L. Shames, A.H. Fairlamb, A. Cerami, C.T. Walsh, Purification and characterization of trypanothione reductase from *Crithidia fasciculata*, a newly discovered member of the family of disulfide-containing flavoprotein reductases, *Biochemistry* 25 (1986) 3519–3526.
- [21] C. Chan, H. Yin, J. Garforth, J.H. McKie, R. Jaouhari, P. Speers, K.T. Douglas, P. J. Rock, V. Yardley, S.L. Croft, A.H. Fairlamb, Phenothiazine inhibitors of trypanothione reductase as potential antitrypanosomal and antileishmanial drugs, *J. Med. Chem.* 41 (1998) 148–156.
- [22] P. Baiocco, G. Poce, S. Alfonso, M. Cocozza, G.C. Porretta, G. Colotti, M. Biava, F. Moraca, M. Botta, V. Yardley, A. Fiorillo, A. Lantella, F. Malatesta, A. Ilari, Inhibition of *Leishmania infantum* trypanothione reductase by azole-based compounds: a comparative analysis with its physiological substrate by X-ray crystallography, *ChemMedChem* 8 (2013) 1175–1183.
- [23] R. De Gasparo, E. Brodbeck-Persch, S. Bryson, N.B. Hentzen, M. Kaiser, E.F. Pai, R. L. Krauth-Siegel, F. Diederich, Biological evaluation and X-ray co-crystal structures of cyclohexylpyrrolidine ligands for trypanothione reductase, an enzyme from the redox metabolism of *Trypanosoma*, *ChemMedChem* 13 (2018) 957–967.
- [24] A.K. Shukla, S. Patra, V.K. Dubey, Evaluation of selected antitumor agents as subversive substrate and potential inhibitor of trypanothione reductase: an alternative approach for chemotherapy of Leishmaniasis, *Mol. Cell. Biochem.* 352 (2011) 261–270.
- [25] M.A. Toro, P.A. Sanchez-Murcia, D. Moreno, M. Ruiz-Santaquiteria, J.F. Alzate, A. Negri, M.J. Camarasa, F. Gago, S. Velazquez, A. Jimenez-Ruiz, Probing the dimerization interface of *Leishmania infantum* trypanothione reductase with site-directed mutagenesis and short peptides, *Chembiochem* 14 (2013) 1212–1217.
- [26] H. de Lucio, M.A. Toro, M.J. Camarasa, S. Velazquez, F. Gago, A. Jimenez-Ruiz, Pseudoirreversible slow-binding inhibition of trypanothione reductase by a protein-protein interaction disruptor, *Br. J. Pharmacol.* 177 (2020) 5163–5176.
- [27] A. Revuelto, H. de Lucio, J.C. Garcia-Soriano, P.A. Sanchez-Murcia, F. Gago, A. Jimenez-Ruiz, M.J. Camarasa, S. Velazquez, Efficient dimerization disruption of *Leishmania infantum* trypanothione reductase by triazole-phenyl-thiazoles, *J. Med. Chem.* 64 (2021) 6137–6160.
- [28] S.S. Khan, S. Hanelt, J. Liebscher, Versatile synthesis of 1,2,3-triazolium-based ionic liquids, *ARKIVOC* (Gainesville, FL, U. S.) 2009 (2009) 193–208.
- [29] J.M. Aizpurua, R.M. Fratila, Z. Monasterio, N. Perez-Esnaola, E. Andreieff, A. Irazorza, M. Sagartazu-Aizpurua, Triazolium cations: from the "click" pool to multipurpose applications, *New J. Chem.* 38 (2014) 474–480.
- [30] R. Mishra, J.S. Mishra, S.A. Chaubey, Recent advances on triazolium ionic liquids: synthesis and applications, *Curr. Org. Chem.* 23 (2019) 1239–1255.
- [31] I. Steiner, N. Stojanovic, A. Bolje, A. Brozovic, D. Polancec, A. Ambriovic-Ristov, M.R. Stojkovic, I. Piantanida, D. Eljuga, J. Kosmrli, M. Osmak, Discovery of 'click' 1,2,3-triazolium salts as potential anticancer drugs, *Radiol. Oncol.* 50 (2016) 280–288.
- [32] E.M. de Souza-Fagundes, J. Delp, P.H.D.M. Prazeres, L.B. Marques, A.M.L. Carmo, P.H.F. Stroppa, N. Glanzmann, J. Kisitu, D. Szamosvari, T. Botcher, M. Leist, A. D. da Silva, Correlation of structural features of novel 1,2,3-triazoles with their neurotoxic and tumoricidal properties, *Chem. Biol. Interact.* 291 (2018) 253–263.
- [33] R. Wang, Y. Li, W. Dehaen, Antiproliferative effect of mitochondria-targeting allobetulin 1,2,3-triazolium salt derivatives and their mechanism of inducing apoptosis of cancer cells, *Eur. J. Med. Chem.* 207 (2020), 112737.
- [34] J.T. Fletcher, J.M. Sobczyk, S.C. Gwazdzac, A.J. Blanck, Antimicrobial 1,3,4-trisubstituted-1,2,3-triazolium salts, *Bioorg. Med. Chem. Lett.* 28 (2018) 3320–3323.
- [35] Q. Li, L.S.S. Qiu, W.Q. Tan, G.D. Gu, Z.Y. Guo, Novel 1,2,3-triazolium-functionalized inulin derivatives: synthesis, free radical-scavenging activity, and antifungal activity, *RSC Adv.* 7 (2017) 42225–42232.
- [36] P.H.F. Stroppa, L.M.R. Antinarelli, A.M.L. Carmo, J. Gameiro, E.S. Coimbra, A. D. da Silva, Effect of 1,2,3-triazole salts, non-classical bioisosteres of miltefosine, on *Leishmania amazonensis*, *Bioorg. Med. Chem.* 25 (2017) 3034–3045.
- [37] R.S. Meinel, A.D.C. Almeida, P.H.F. Stroppa, N. Glanzmann, E.S. Coimbra, A.D. da Silva, Novel functionalized 1,2,3-triazole derivatives exhibit antileishmanial activity, increase in total and mitochondrial-ROS and depolarization of mitochondrial membrane potential of *Leishmania amazonensis*, *Chem. Biol. Interact.* 315 (2020), 108850.
- [38] M. M'Sahel, M.M. Obadia, R. Medimagh, A. Serghei, M.S. Zina, E. Drockenmuller, Biosourced 1,2,3-triazolium ionic liquids derived from isosorbide, *New J. Chem.* 40 (2016) 740–747.

- [39] F. Zapata, L. Gonzalez, A. Caballero, I. Alkorta, J. Elguero, P. Molina, Dual role of the 1,2,3-triazolium ring as a hydrogen-bond donor and anion- $\pi$  receptor in anion-recognition processes, *Chem. Eur. J.* 21 (2015) 9797–9808.
- [40] Z. Monasterio, M. Sagartzazu-Aizpurua, J.I. Miranda, Y. Reyes, J.M. Aizpurua, Cationic 1,2,3-triazolium alkynes: components to enhance 1,4-regioselective azide-alkyne cycloaddition reactions, *Org. Lett.* 18 (2016) 788–791.
- [41] A. Helal, H.G. Kim, M.K. Ghosh, C.H. Choi, S.H. Kim, H.S. Kim, New regioisomeric naphthol thiazole based 'turn-on' fluorescent chemosensor for  $Al^{3+}$ , *Tetrahedron* 69 (2013) 9600–9608.
- [42] S. Rudolph, H. Dahlhaus, W. Hanekamp, C. Albers, M. Barth, G. Michels, D. Friedrich, M. Lehr, Aryl N-[ $\omega$ -(6-fluorindol-1-yl)alkyl]carbamates as inhibitors of fatty acid amide hydrolase, monoacylglycerol lipase, and butyrylcholinesterase: structure-activity relationships and hydrolytic stability, *ACS Omega* 6 (2021) 13466–13483.
- [43] P. Gilles, R.S. Kashyap, M.J. Freitas, S. Ceusters, K. Van Asch, A. Janssens, S. De Jonghe, L. Persoons, M. Cobbaut, D. Daelemans, J. Van Lint, A.R.D. Voet, W.M. De Borggraeve, Design, synthesis and biological evaluation of pyrazolo[3,4-d]pyrimidine-based protein kinase D inhibitors, *Eur. J. Med. Chem.* 205 (2020), 112638.
- [44] R.A. Copeland, *Enzymes, A Practical Introduction to Structure, Mechanism, and Data Analysis*, second ed., Wiley-VCH, Inc., New York, 2002.
- [45] R.A. Copeland, *Evaluation of Enzyme Inhibitors in Drug Discovery: a Guide for Medicinal Chemists and Pharmacologists*, second ed., John Wiley & Sons, Inc., Hoboken, NJ, 2013.
- [46] C.S. Bond, Y. Zhang, M. Berriman, M.L. Cunningham, A.H. Fairlamb, W.N. Hunter, Crystal structure of *Trypanosoma cruzi* trypanothione reductase in complex with trypanothione, and the structure-based discovery of new natural product inhibitors, *Structure* 7 (1999) 81–89.
- [47] A. Saravanamuthu, T.J. Vickers, C.S. Bond, M.R. Peterson, W.N. Hunter, A. H. Fairlamb, Two interacting binding sites for quinacrine derivatives in the active site of trypanothione reductase: a template for drug design, *J. Biol. Chem.* 279 (2004) 29493–29500.
- [48] R. De Gasparo, O. Halgas, D. Harangozo, M. Kaiser, E.F. Pai, R.L. Krauth-Siegel, F. Diederich, Targeting a large active site: structure-based design of nanomolar inhibitors of trypanosoma brucei trypanothione reductase, *Chem. Eur. J.* 25 (2019) 11416–11421.
- [49] A. Revuelto, M. Ruiz-Santaquiteria, H. de Lucio, A. Gamó, A.A. Carriles, K. J. Gutierrez, P.A. Sanchez-Murcia, J.A. Hermoso, F. Gago, M.J. Camarasa, A. Jimenez-Ruiz, S. Velazquez, Pyrrolopyrimidine vs imidazole-phenyl-thiazole scaffolds in nonpeptidic dimerization inhibitors of *Leishmania infantum* trypanothione reductase, *ACS Infect. Dis.* 5 (2019) 873–891.
- [50] A. Baici, *Kinetics of Enzyme-Modifier Interactions Selected Topics in the Theory and Diagnosis of Inhibition and Activation Mechanisms*, first ed., Springer-Verlag, Vienna, Austria, 2015.
- [51] A. Rashid, A. Vakurov, S. Mohamadi, D. Sanver, A. Nelson, Substituents modulate biphenyl penetration into lipid membranes, *Biochim. Biophys. Acta-Biomembr.* 1859 (2017) 712–721.
- [52] R.F. Sweis, Target (in)validation: a critical, sometimes unheralded, role of modern medicinal chemistry, *ACS Med. Chem. Lett.* 6 (2015) 618–621.
- [53] M.R. Ariyanayagam, A.H. Fairlamb, Ovothiol and trypanothione as antioxidants in trypanosomatids, *Mol. Biochem. Parasitol.* 115 (2001) 189–198.
- [54] S. Wyllie, M.L. Cunningham, A.H. Fairlamb, Dual action of antimonial drugs on thiol redox metabolism in the human pathogen *Leishmania donovani*, *J. Biol. Chem.* 279 (2004) 39925–39932.
- [55] S. Krieger, W. Schwarz, M.R. Ariyanayagam, A.H. Fairlamb, R.L. Krauth-Siegel, C. Clayton, Trypanosomes lacking trypanothione reductase are avirulent and show increased sensitivity to oxidative stress, *Mol. Microbiol.* 35 (2000) 542–552.
- [56] D.P. Weldrick, B. Chodacka, R. Vogt, D.J. Steenkamp, The effect of buthionine sulfoximine on the growth of *Leishmania donovani* in culture, *FEMS Microbiol. Lett.* 173 (1999) 139–146.
- [57] O.W. Griffith, Mechanism of action, metabolism, and toxicity of buthionine sulfoximine and its higher homologs, potent inhibitors of glutathione synthesis, *J. Biol. Chem.* 257 (1982) 13704–13712.
- [58] C. Vazquez, M. Mejia-Tlachi, Z. Gonzalez-Chavez, A. Silva, J.S. Rodriguez-Zavala, R. Moreno-Sanchez, E. Saavedra, Buthionine sulfoximine is a multitarget inhibitor of trypanothione synthesis in *Trypanosoma cruzi*, *FEBS Lett.* 591 (2017) 3881–3894.
- [59] W. Kabsch, XDS, *Acta Crystallogr. Sect. D Biol. Crystallogr.* 66 (2010) 125–132.
- [60] M.D. Winn, C.C. Ballard, K.D. Cowtan, E.J. Dodson, P. Emsley, P.R. Evans, R. M. Keegan, E.B. Krissinel, A.G. Leslie, A. McCoy, S.J. McNicholas, G.N. Murshudov, N.S. Pannu, E.A. Potterton, H.R. Powell, R.J. Read, A. Vagin, K.S. Wilson, Overview of the CCP4 suite and current developments, *Acta Crystallogr. Sect. D Biol. Crystallogr.* 67 (2011) 235–242.
- [61] P.R. Evans, G.N. Murshudov, How good are my data and what is the resolution? *Acta Crystallogr. Sect. D Biol. Crystallogr.* 69 (2013) 1204–1214.
- [62] A. Vagin, A. Teplyakov, Molecular replacement with MOLREP, *Acta Crystallogr. Sect. D Biol. Crystallogr.* 66 (2010) 22–25.
- [63] G.N. Murshudov, P. Skubak, A.A. Lebedev, N.S. Pannu, R.A. Steiner, R.A. Nicholls, M.D. Winn, F. Long, A.A. Vagin, REFMAC5 for the refinement of macromolecular crystal structures, *Acta Crystallogr. Sect. D Biol. Crystallogr.* 67 (2011) 355–367.
- [64] P. Emsley, K. Cowtan, Coot: model-building tools for molecular graphics, *Acta Crystallogr. Sect. D Biol. Crystallogr.* 60 (2004) 2126–2132.
- [65] C.J. Hamilton, A. Saravanamuthu, I.M. Eggleston, A.H. Fairlamb, Ellman's-reagent-mediated regeneration of trypanothione in situ: substrate-economical microplate and time-dependent inhibition assays for trypanothione reductase, *Biochem. J.* 369 (2003) 529–537.
- [66] L.L.C. Schrodinger, The PyMOL Molecular Graphics System, Version 1.8, 2015.
- [67] J. Klett, A. Nunez-Salgado, H.G. Dos Santos, A. Cortes-Cabrera, A. Perona, R. Gil-Redondo, D. Abia, F. Gago, A. Morreale, MM-ISMSA: an ultrafast and accurate scoring function for protein-protein docking, *J. Chem. Theor. Comput.* 8 (2012) 3395–3408.
- [68] C. Tian, K. Kasavajhala, K.A.A. Belfon, L. Raguette, H. Huang, A.N. Miguez, J. Bickel, Y. Wang, J. Pincay, Q. Wu, C. Simmerling, ff19SB: amino-acid-specific protein backbone parameters trained against quantum mechanics energy surfaces in solution, *J. Chem. Theor. Comput.* 16 (2020) 528–552.
- [69] S. Izadi, R. Anandakrishnan, A.V. Onufriev, Building water models: a different approach, *J. Phys. Chem. Lett.* 5 (2014) 3863–3871.
- [70] D.A. Case, H.M. Aktulga, K. Belfon, I.Y. Ben-Shalom, S.R. Brozell, D.S. Cerutti, T. E. Cheatham III, G.A. Cisneros, V.W.D. Cruzeiro, T.A. Darden, R.E. Duke, G. Giambasu, M.K. Gilson, H. Gohlke, A.W. Goetz, R. Harris, S. Izadi, S.A. Izmailov, C. Jin, K. Kasavajhala, M.C. Kaymak, E. King, A. Kovalenko, T. Kurtzman, T.S. Lee, S. LeGrand, P. Li, C. Lin, J. Liu, T. Luchko, R. Luo, M. Machado, V. Man, M. Manathunga, K.M. Merz, Y. Miao, O. Mikhailovskii, G. Monard, H. Nguyen, K. A. O'Hearn, A. Onufriev, F. Pan, S. Pantano, R. Qi, A. Rahnamoun, D.R. Roe, A. Roitberg, C. Sagui, S. Schott-Verdugo, J. Shen, C.L. Simmerling, N. R. Skrynnikov, J. Smith, J. Swails, R.C. Walker, J. Wang, H. Wei, R.M. Wolf, X. Wu, Y. Xue, D.M. York, S. Zhao, P.A. Kollman, Amber 2021, in: University of California, San Francisco, 2021.
- [71] T.S. Lee, B.K. Radak, A. Pabis, D.M. York, A new maximum likelihood approach for free energy profile construction from molecular simulations, *J. Chem. Theor. Comput.* 9 (2013) 153–164.